Supplementary Information

Supplementary Methods

Synthesis of ^{89}Zr-DFO-SC16-NS and ^{89}Zr-DFO-SC16-SS:

The non-site-selectively modified SC16-based immunoconjugate (DFO-SC16-NS) was produced by incubating 6 molar equivalents of an amine-reactive bi-functional chelator – *p*-isothiocyanatobenzoyl desferrioxamine (*p*-SCN-DFO, Macrocyclics, Inc.) with 1 molar equivalent of the SC16 antibody under slightly basic conditions (pH 8.5 – 8.7) at 25°C for 90 min. The site-selectively modified SC16-based immunoconjugate (DFO-SC16-SS) was produced after performing a reduction of the site-selectively engineered SC16 antibody with 10 molar equivalents of tris(2-carboxyethyl) phosphine (TCEP, Pierce) for 1 h, followed by the incubation of the reduced antibody with 10 molar equivalents of a thiol-reactive maleimido-desferrioxamine (Mal-DFO, Macrocyclics, Inc.) at 25°C for 1 h. The immunoconjugates were purified by size exclusion chromatography using PD-10 desalting columns (Sephadex G-25 M, GE Healthcare). The average number of chelators per antibody in the immunoconjugate preparations was determined via intact protein LC-MS analysis. The immunoconjugates were evaluated in surface plasmon resonance experiments to ascertain the immunoreactivity and binding affinity to DLL3. High specific activity radioimmunoconjugates (and) were prepared using previously described methods (1). The purity of the radioimmunoconjugate preparation was assayed by radio-TLC and the radioimmunoconjugates were tested for antibody stability and demetallation of $^{89}Zr^{4+}$ by incubating in human AB-type serum for 5 days at 37°C and assaying the radiochemical purity via radio-TLC. Next, 100-200 μg of the SC16-immunoconjugates were incubated with pH-adjusted ^{89}Zr (37-74 MBq; 1-2 mCi) for 1 h at 25°C. The reaction progress was assayed via radio-thin layer chromatography (radio-TLC) on silica-impregnated paper using an eluent of 50 mM EDTA, pH 5. In radio-TLC analyses, the radiolabeled antibody construct should remain at the baseline, while $^{89}Zr^{4+}$ ions and ^{89}Zr-EDTA elutes with the solvent front. After 1 h, the reaction was quenched with EDTA and the radioimmunoconjugates were purified using a PD-10 desalting column for size-exclusion chromatography.

Cell lines

All cell lines used in this study were obtained from the American Type Culture Collection and grown under aseptic conditions in an incubator providing humidified atmosphere of 5% CO_2 in air. H82 and H69 cells were cultured in RPMI base media supplemented with 10% fetal bovine serum, 2 mM L-glutamine, 10 mM HEPES, 1 mM sodium pyruvate, 4,500 mg/L glucose, 1500 mg/L sodium bicarbonate and 100 U/mL penicillin and 100 µg/mL streptomycin. To facilitate the *in vivo* visualization and assessment of the growth and spread of tumor cells in orthotopic and metastatic tumor models for SCLC, H82 cells were transduced with firefly luciferase in the pLENTI6 lentiviral transfer vector (Invitrogen). After blasticidin selection, the resulting cell line, luc-H82, was used for *in vivo* bioluminescence imaging experiments. A549 cells were cultured in F-12K base media supplemented with 10% fetal bovine serum and 100 U/mL penicillin and 100 µg/mL streptomycin.

Immunohistochemistry

Immunohistochemistry was performed to assess DLL3 expression in xenograft tumors. Formalin-fixed paraffin-embedded tissues from H82, H69 and A549 tumors were sectioned onto slides and were deparaffinized, rehydrated, and treated with an antigen retrieval solution (S1700, DAKO USA, Carpinteria, CA) for 20min at 99°C. After washing, the slides were blocked with avidin, biotin blocking kit (Vector laboratories, Burlingame, CA), and 10% horse serum in 3% bovine serum albumin in TBS. Anti-human DLL3 (at 10µg/ml, SC16.65, StemCentrx, South San Francisco, CA) was applied on the slides and incubated for 1 hour at room temperature, followed by horse anti-mouse biotinylated antibody (Vector laboratories) and ABC Elite (Vector laboratories) incubation. Mouse IgG2a was used for isotype control. Signal detection was done with DAB and slides were counterstained with hematoxylin prior to adding the coverslip onto the tissue section. The stained slides were scanned with a Leica slide scanner (Leica Biosystems, Buffalo Grove, IL) using a 20X objective lens and scored by a pathologist.

In vitro saturation binding assay

The cell binding activity of the ^{89}Zr-DFO-SC16-NS for DLL3 expressed on SCLC cells was confirmed using an *in vitro* antigen saturation-binding assay. To this end, a 0.4 μg/mL solution of ^{89}Zr-DFO-SC16-NS was prepared in PBS supplemented with 1% BSA. Twenty microliters of the radioimmunoconjugate solution was added to a microcentrifuge tube containing 50 x 10^6 cells in 1 mL of culture media. The resulting mixture was incubated for 1 h on ice with intermittent tapping to resuspend the cells. Thereafter, the cells were pelleted via centrifugation (600 x g for 3 min), and the supernatant was pipetted out in to a separate microcentrifuge tube. The cells were washed with 1 mL of ice-cold PBS, and centrifuged (600 × g for 3 min) before pipetting out the supernatant to another centrifuge tube. This washing procedure was repeated two more times. Finally, the cell pellet, the media supernatant, and the three wash fractions were measured for radioactivity on a gamma counter calibrated for ^{89}Zr. The percentage of cell bound radioactivity of the radioimmunoconjugate was determined using the formula:

$$\text{Immunoreactive Fraction} = [\text{Counts}_{\text{Cell Pellet}}]/[[\text{Counts}_{\text{Cell Pellet}} + \text{Counts}_{\text{Media Supernatant}} + \text{Counts}_{\text{Wash1}} + \text{Counts}_{\text{Wash2}} + \text{Counts}_{\text{Wash3}}]$$

Xenograft Models

To develop the subcutaneous and the orthotopic lung xenograft models, 6-8 week old female athymic nude mice (01B74-Athymic NCr-nu/nu; Charles River Laboratories, NY, USA) were obtained and allowed to acclimatize at the Memorial Sloan Kettering Cancer Center vivarium for 1 week with food and water being provided *ad libitum* prior to the implantation of the tumor cells. Briefly, for subcutaneous xenograft models of H82 and H69 tumors, 3 million cells were suspended in 150 μL of 1:1 media/matrigel basement membrane matrix (BD Biosciences) and injected subcutaneously on the right shoulder of each mouse. Similarly, 5 million A549 cells were injected per mouse to develop a subcutaneous xenograft model for A549 tumors. The mice were used for PET imaging and acute biodistribution studies within 2-5 weeks after xenografting, when the tumors reached a volume of ~ 200 – 250 mm^3. To develop an orthotopic xenograft model of SCLC, mice were anesthetized using isoflurane and 1.5 – 3 million luc-H82 cells were suspended

in 10 μL of sterile phosphate buffered saline (PBS) and surgically implanted on the left lung under aseptic conditions. The orthotopic tumor take-rate and growth was monitored on a weekly basis by intraperitoneal injection of luciferin substrate followed by bioluminescence imaging in an IVIS Spectrum optical imaging suite (Perkin Elmer). The mice were used for PET imaging and biodistribution studies 5 – 8 weeks after orthotopic implantation of the luc-H82 tumor cells.

Further, the clinical utility of ^{89}Zr-DFO-SC16-SS to predict response to therapy with DLL3-targeted agents such as SC16LD6.5, was assessed by using 3 PDX lines – Lu64 (high DLL3 expression, complete response to treatment with SC16-T), Lu149 (moderate DLL3 expression, complete response to treatment with SC16-T followed by relapse) and Lu80 (low DLL3 expression, minimal response to treatment with SC16-T). The PDX tumors were passaged in mice and prepared as single cell suspensions using a gentleMACS™ dissociator (Miltenyi Biotec) prior to subcutaneous transplantation on the right shoulders of athymic nude mice. The mice were used for PET imaging and biodistribution studies 5 – 6 weeks after the subcutaneous transplantation, when the tumors reached a volume of ~ 120-150 mm^3.

Finally, an animal model was developed to recapitulate distant organ metastases of SCLC via an intracardiac injection of 1.5 – 2 million luc-H82 cells in NSG (NOD.Cg-Prkdc{scid Il2rg{tm1Wjl}/SzJ) mice (Jackson laboratories, USA) (n=16 mice). As such, the intracardiac injection is expected to promote the seeding of the tumor cells in the liver and bones of these animals. The animals were monitored for metastatic seeding and growth of tumor cells via bioluminescence imaging using an IVIS Spectrum optical imaging suite (Perkin Elmer). PET imaging and biodistribution studies were carried out at 2.5 weeks after the intracardiac injection of the luc-H82 tumor cells, when the mice in this experimental cohort were found to be active with no apparent indications of the tumor burden overbearing their physiological health and/or physical appearance.

PET Imaging

A minimum of 20 million coincident events was recorded for each scan, which lasted between 10-45 min. An energy window of 350-700 keV and a coincidence-timing window of 6 ns were used. The counting rates in the reconstructed images were converted to

activity concentrations (percentage injected dose [%ID] per gram of tissue) by use of a system calibration factor derived from the imaging of a mouse-sized water-equivalent phantom containing ^{89}Zr. Data were sorted into 2-dimensional histograms by Fourier re-binning, and transverse images were reconstructed by filtered back-projection (FBP) into a 128 × 128 × 63 (0.72 × 0.72 × 1.3 mm) matrix. The image data were normalized to correct for non-uniformity of response of the PET, dead-time count losses, positron branching ratio, and physical decay to the time of injection, but no attenuation, scatter, or partial-volume averaging correction was applied. Two-dimensional regions of interest (2D ROIs) were drawn over the tumor margins in all coronal planes of the PET image to obtain a statistically relevant tumor uptake (% ID/g) of the radioimmunoconjugate in the tumor.

Biodistribution Studies

For biodistribution studies, the tumor-bearing mice were warmed gently under a heat lamp for 5 min before administration of the appropriate ^{89}Zr-DFO-immunoconjugate [0.74 – 1.11 MBq (20-30 μCi); 2.5-3.75 μg in 200 μL chelexed PBS,] via intravenous tail vein injection (t = 0). Animals (n = 4 per group) were euthanized by CO_2(g) asphyxiation at 24, 48, 72, 96, and 120 h post-injection. To probe the ability to saturate the target antigen – DLL3, an additional cohort of animals was administered ^{89}Zr-DFO-SC16-SS/NS with dramatically lowered specific activity — achieved via co-injection of the standard biodistribution dose of the radioimmunoconjugate mixed with a 100-fold excess of the cold, unlabeled SC16 antibody — and euthanized at 72 h post-injection of the prepared mixture. After asphyxiation, relevant tissues (including the tumor) were removed, rinsed in water, dried in air for 5 min, weighed, and counted in a gamma counter calibrated for ^{89}Zr. Counts were converted into activity using a calibration curve generated from known standards. Count data were background- and decay-corrected to the time of injection, and the %ID/g for each tissue sample was calculated by normalization to the total amount of activity injected at t=0.

***Ex vivo* Analyses**

***Ex vivo* ligand binding assays** on frozen tumor tissues were performed as described previously (2, 3). Briefly, the ^{89}Zr-labeled SC16 radioimmunoconjugate was diluted in 170 mM Tris-HCL (pH 7.5), and applied to fresh-frozen tumor sections (10 μm)

for 1 hour at room temperature in a humidified chamber. Following three washes with PBS, the sections were air-dried and exposed to a BAS MS2025 phosphor plate (FujiFilm) for an appropriate length of time, followed by reading on a GE Typhoon 7000IP plate reader. Custom-made ^{89}Zr activity concentration standards were also exposed, to allow the conversion of autoradiographic counts to a molar concentration. Autoradiographic images were analyzed using ImageJ, and ligand-binding parameters were determined using GraphPad Prism 6.02 software.

Autoradiography

After the final time point (120 h p.i.) in the serial PET imaging of mice bearing subcutaneously xenografted H82, H69, Lu64, Lu149 and Lu80 tumors with ^{89}Zr-DFO-SC16-SS, the animals were euthanized via CO_2(g) asphyxiation and the tumors (n=2 per tumor type) were harvested and frozen in optimal cutting temperature (OCT) compound. The frozen tumor tissue was cryosectioned and digital autoradiography was carried out using a GE Typhoon 7000IP with maximum pixel resolution of 25 μm (4). Sequential tumor sections were also analyzed by staining with hematoxylin and eosin (H&E) and the images were captured using a color camera microscope.

Histopathological Analyses of Distant Organ Metastases Model

The tissue samples harvested from the necropsied animals in the metastatic cohort were fixed in 10% neutral buffered formalin for 48 h. Specifically, for examination of the bone tissue, the entire hindleg of the mice including the femur, the knee joint and the tibia was harvested. The bones were decalcified in Surgipath Decalcifier I (Leica) for 3 days. All the tissues were trimmed, routinely processed and embedded in paraffin. 4 μm sections were cut and stained with Hematoxylin and Eosin (H&E) for morphologic evaluation.

The slides were first examined by a board-certified veterinary pathologist (AP) in a blinded fashion. The presence of neoplastic cells was documented and classified into metastasis when the growth of malignant cells was clearly infiltrating and effacing the affected organ, or as embolus when local invasion was not a feature. A semi-quantitative score for tumor burden in the liver was obtained by applying a 2-tier system as shown below:

Tier 1	Number of metastases = 1 to 3 per lobe		Number of metastases = >3 per lobe
	not in all lobes	in all lobes	
	1	2	3
Tier 2	Effaced parenchyma <30%	Effaced parenchyma 30 to 50%	Effaced parenchyma >50%
	1	2	3

The tier-1 score assigned a numeric value depending on the average number of metastases per lobe and their overall distribution in the liver. A second level (tier-2) considered the percentage of parenchyma effaced by the neoplastic population. The total score resulted from the sum of the individual scores per animal. To correlate the histopathologically observed tumor masses with the resolution of PET imaging, the size of the metastases was estimated subgrossly by measuring the smallest and the largest tumors (the size corresponded to the longest axis as the majority of the masses were rather ovoid in shape).

Supplementary Results:

Fig. S1a

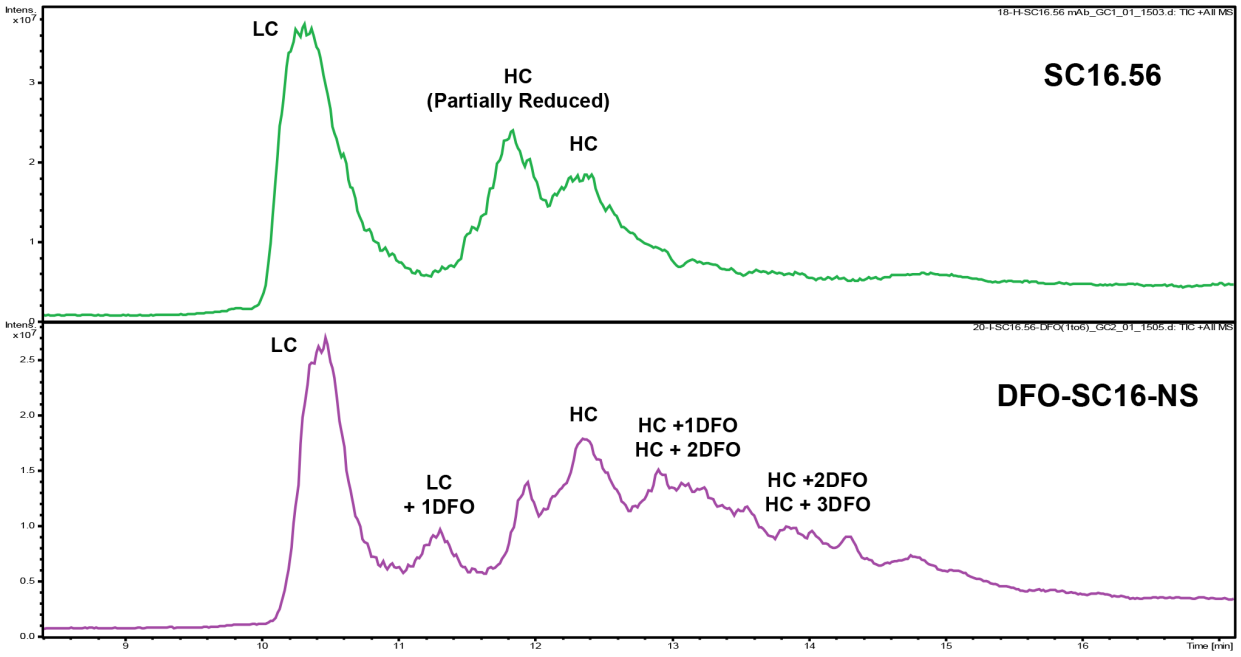

Figure S1a. Size distribution of mass peaks derived from ESI-MS data comparing the unmodified SC16.56 antibody with the non-site-selectively modified DFO-SC16-NS construct. The non-site-selective modification yielded a random distribution of 1-4 DFOs conjugated at different sites available within the light and heavy chains of the SC16.56 antibody.

Fig. S1b

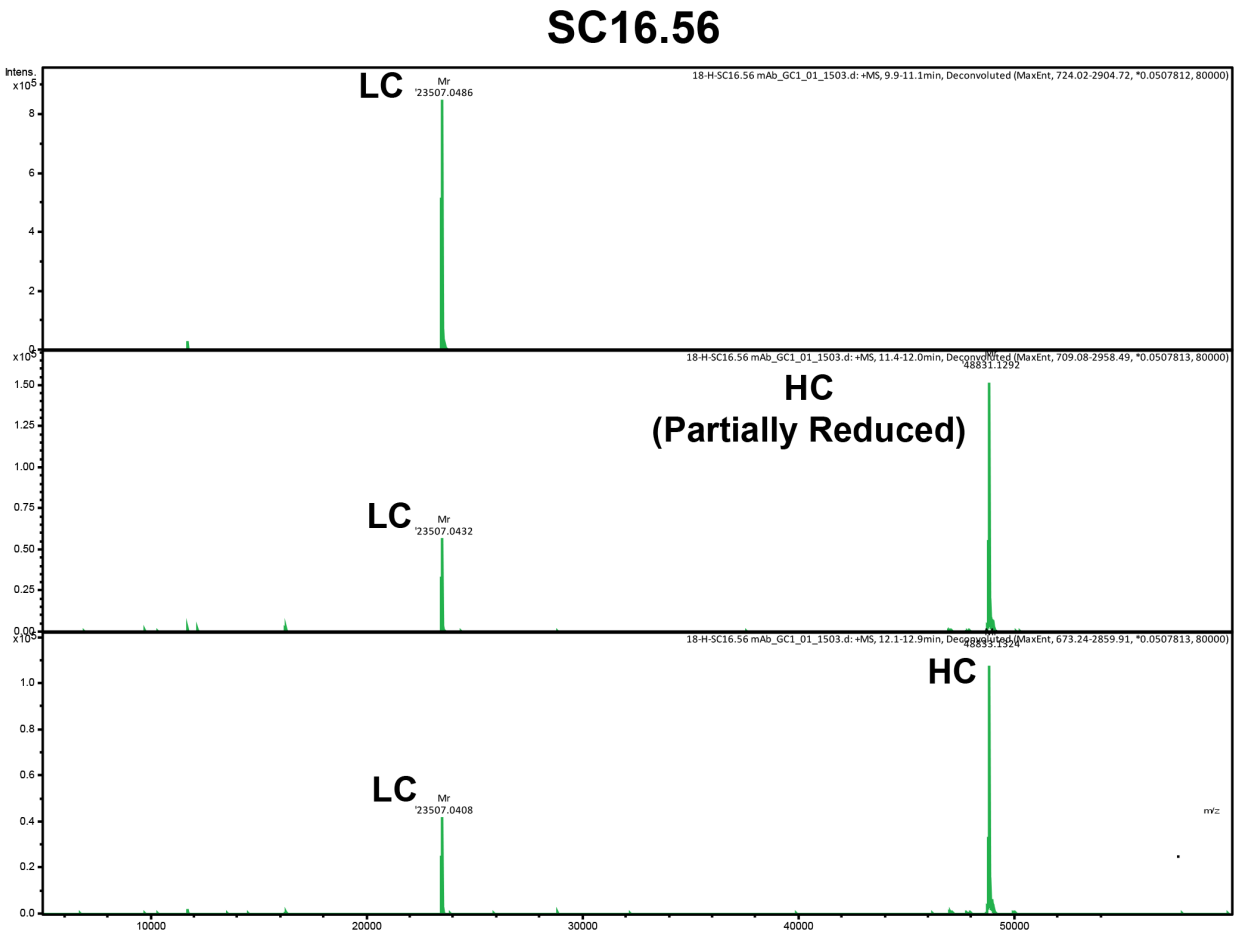

Figure S1b. ESI-MS spectra of the unmodified SC16 antibody. The spectra show peaks corresponding to the mass for the light chain (LC; MW ~ 23,507 Da) and heavy chain (HC; MW ~ 48,833 Da) components of the SC16.56 antibody.

Fig. S1c

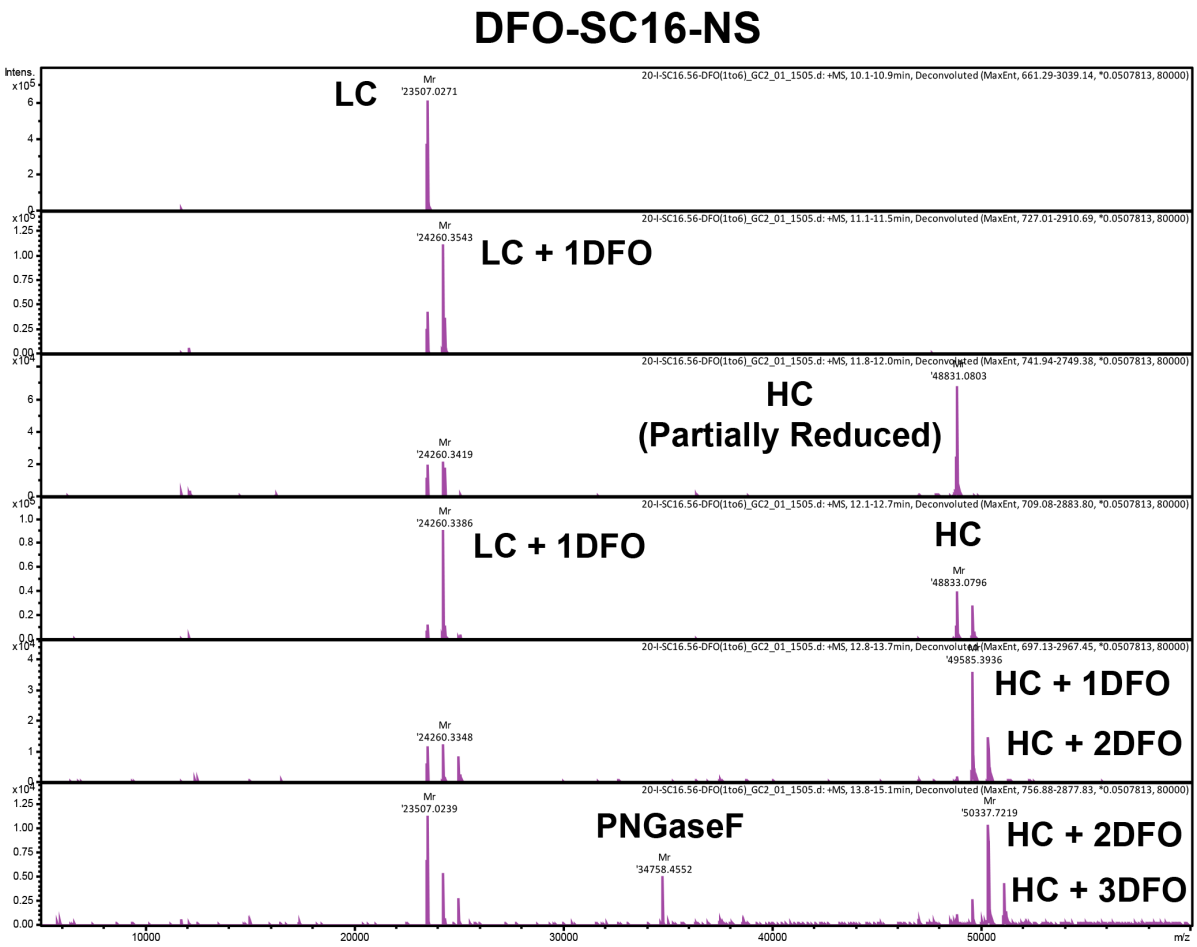

Figure S1c. ESI-MS spectra of the non-site-selectively modified SC16-based immunoconjugate: DFO-SC16-NS. The spectra show peaks corresponding to the masses for the light chain (LC; MW ~ 23,507 Da), the light chain conjugated with 1 DFO (LC + 1DFO; MW ~ 24, 260), the heavy chain (HC; MW ~ 48,833 Da), the heavy chain conjugated with 1-4 DFOs, (HC + 1DFO; MW~ 49,585 Da, HC + 2 DFO; 50, 337 Da) components of the DFO-conjugated SC16 construct.

Fig. S1d

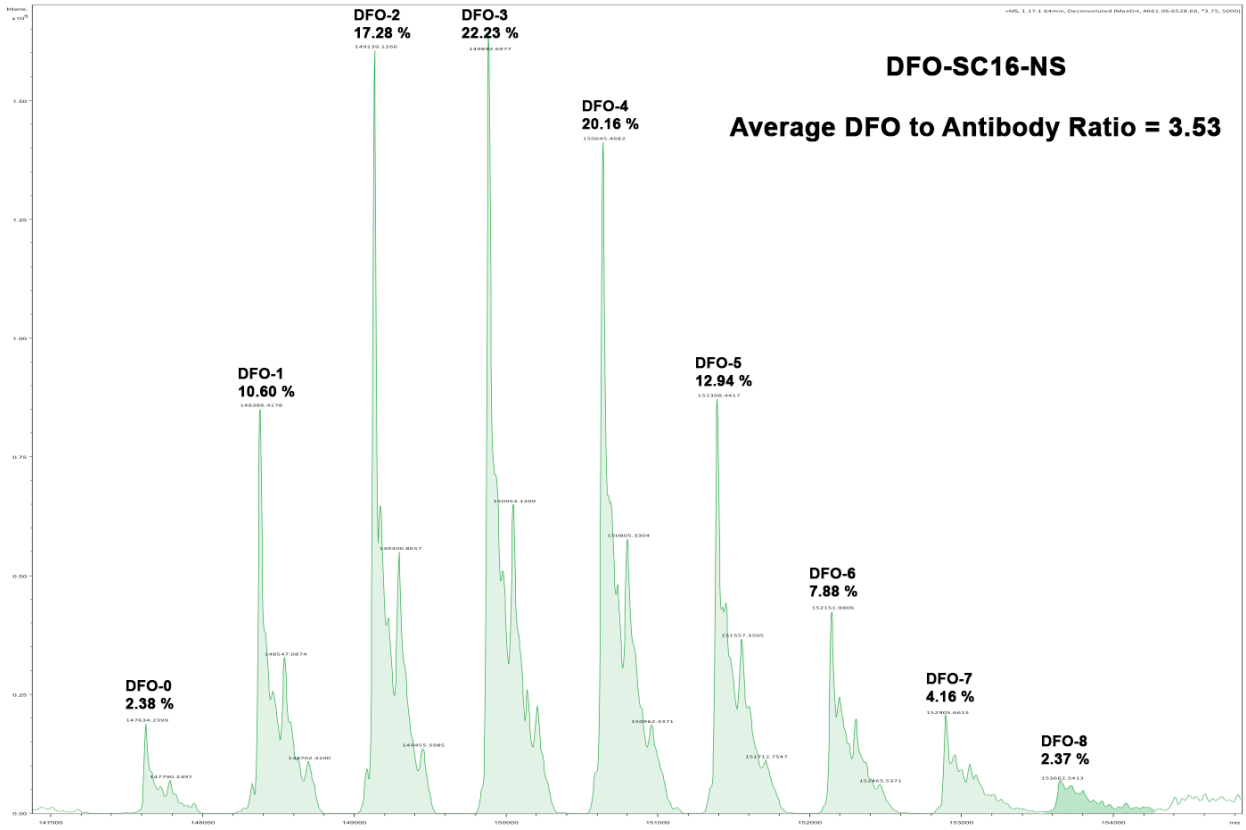

Figure S1d. Native-MS analysis of the non-site-selectively modified SC16-based immunoconjugate: DFO-SC16-NS. The peaks identify the masses within the DFO-SC16-NS construct based on the random conjugation of DFO (left – right: DFO-0 – DFO-8) to lysine residues within the antibody. ~ 60 % of the DFO-SC16-NS construct was found to have between 2-4 DFOs conjugated to the antibody. Overall, this analysis revealed an average of 3.5 DFOs conjugated to antibody in the DFO-SC16-NS construct.

Fig. S2a

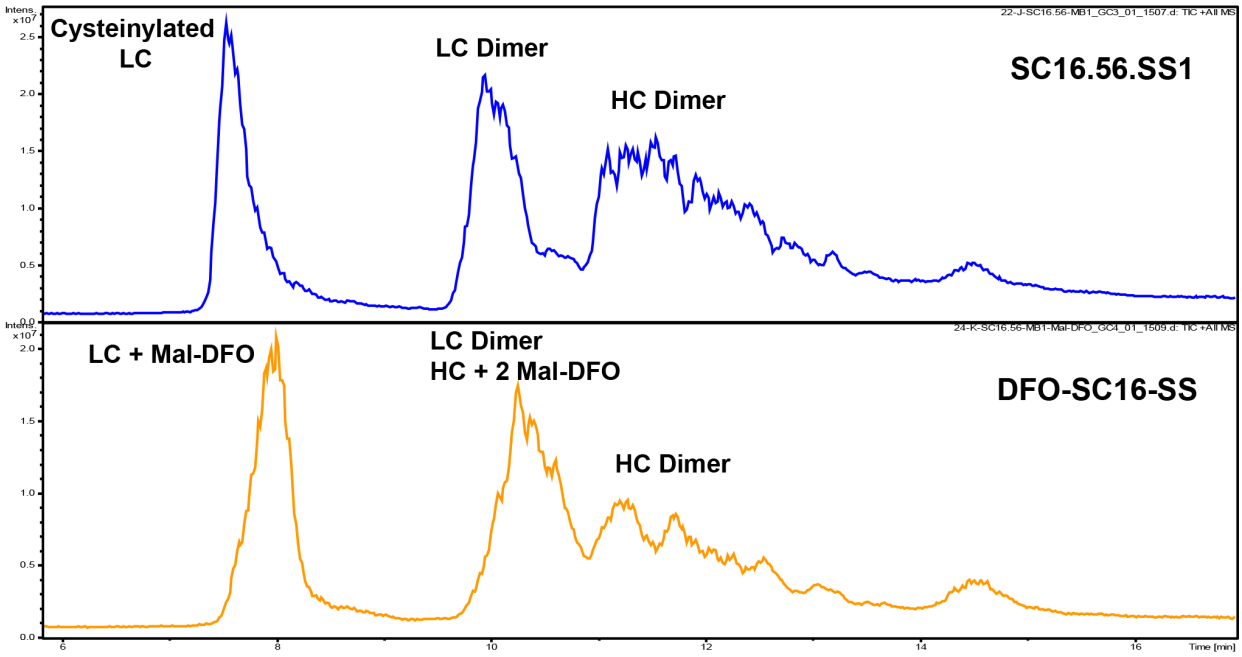

Figure S2a. Size distribution of mass peaks derived from ESI-MS data comparing the unmodified SC16.56.SS antibody with the site-specifically modified DFO-SC16-SS construct. The site-selective modification yielded the conjugation of ~2-6 DFOs per antibody.

Fig. S2b

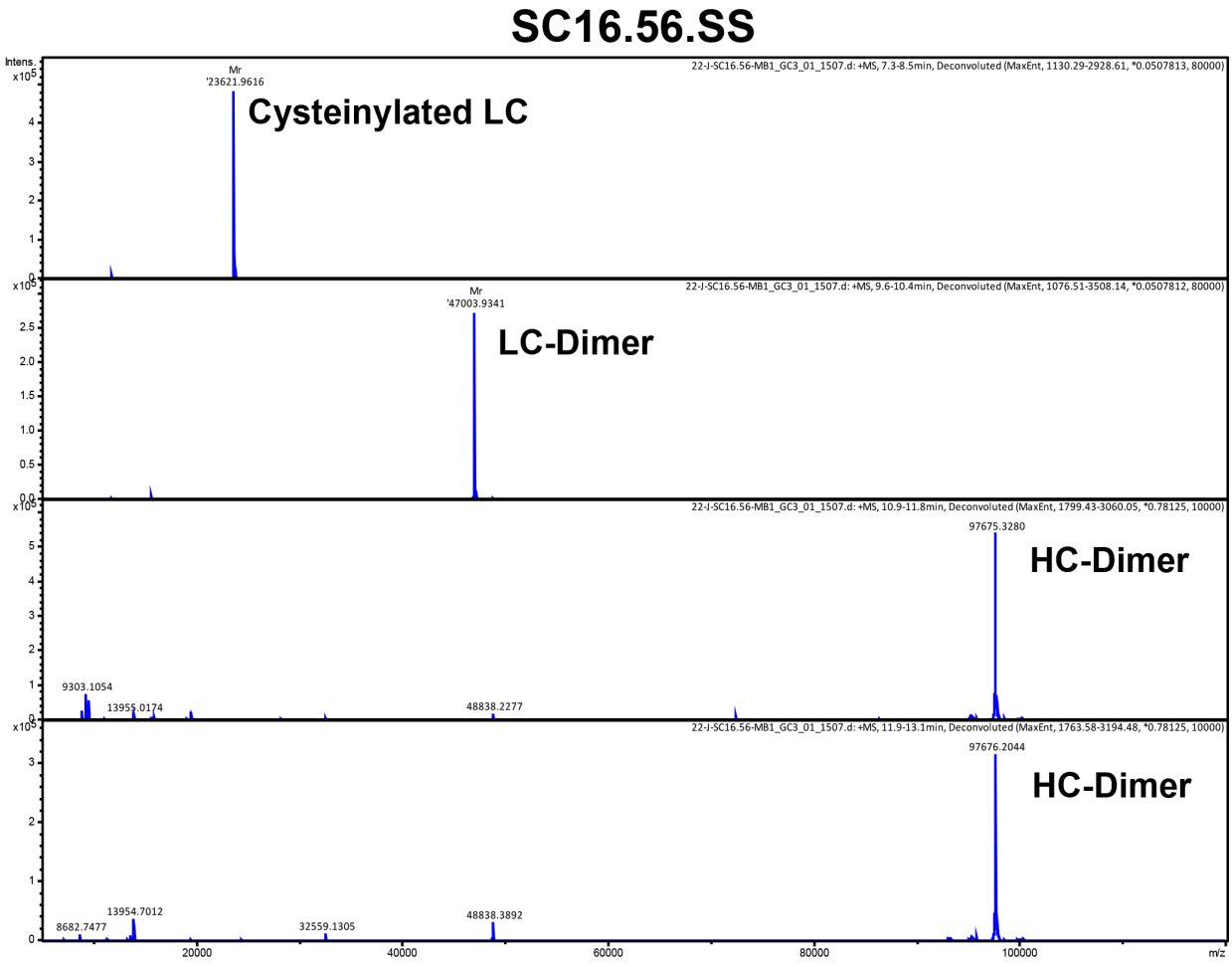

Figure S2b. ESI-MS spectra of the site-specifically engineered SC16.56.SS antibody. The spectra show peaks corresponding to the mass for the cysteinylated light chain (LC; MW ~ 23,622 Da) and its dimer (LC-LC; MW ~ 47,004). Similarly, heavy chain dimers (HC-HC; MW ~ 97,676 Da) were observed for the site-specifically engineered SC16.56.SS antibody.

Fig. S2c

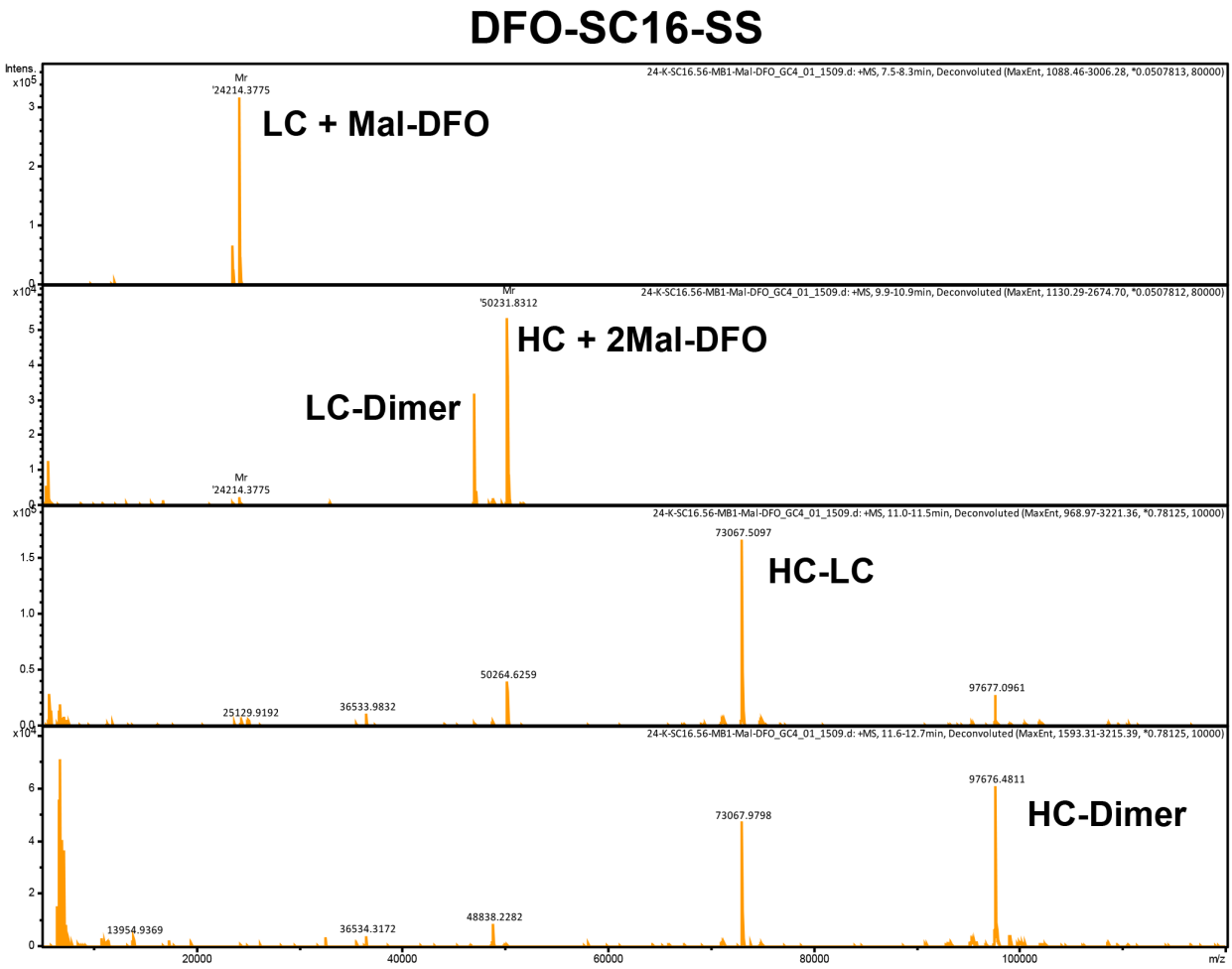

Figure S2c. ESI-MS spectra of the site-selectively modified SC16-based immunoconjugate: DFO-SC16-SS. The spectra show peaks corresponding to the masses for the light chain conjugated with 1 DFO (LC + 1DFO; MW ~ 24, 214), the heavy chain conjugated with 2 DFOs, (HC + 2 DFO; 50, 232 Da) of the DFO-conjugated site-specifically engineered SC16 construct. Additional peaks were also seen for the HC-LC heterodimers (MW ~ 73, 067 Da) and HC-HC homodimers (MW ~ 97, 676 Da).

Fig. S2d

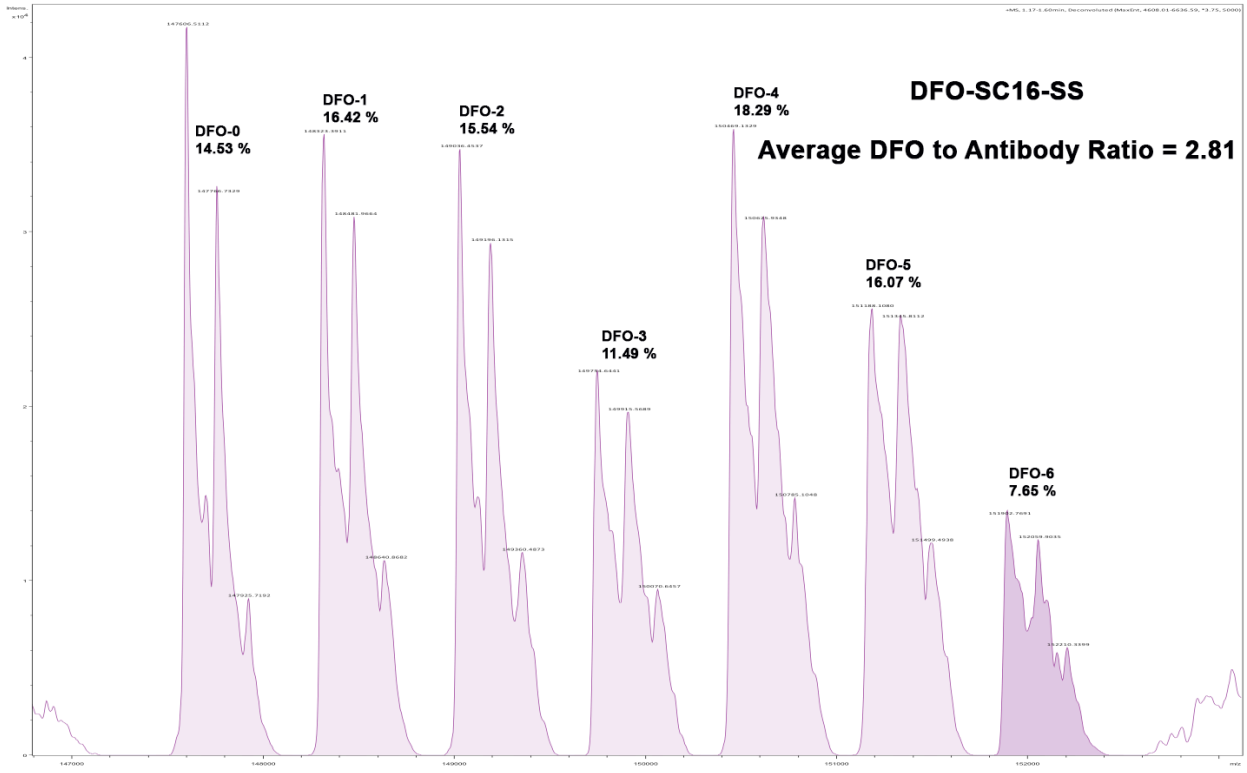

Figure S2d. Native-MS analysis of the site-selectively modified SC16-based immunoconjugate: DFO-SC16-SS. The peaks identify the masses within the DFO-SC16-SS construct based on the site-selective conjugation of DFO (left – right: DFO-0 – DFO-6) to reduced cysteine residues within the light and heavy chain domains in the hinge region of the antibody. ~ 60 % of the DFO-SC16-SS construct was found to have between 1-4 DFOs conjugated to the antibody. Overall, this analysis revealed an average of 2.8 DFOs conjugated to antibody in the DFO-SC16-SS construct.

Fig. S3a

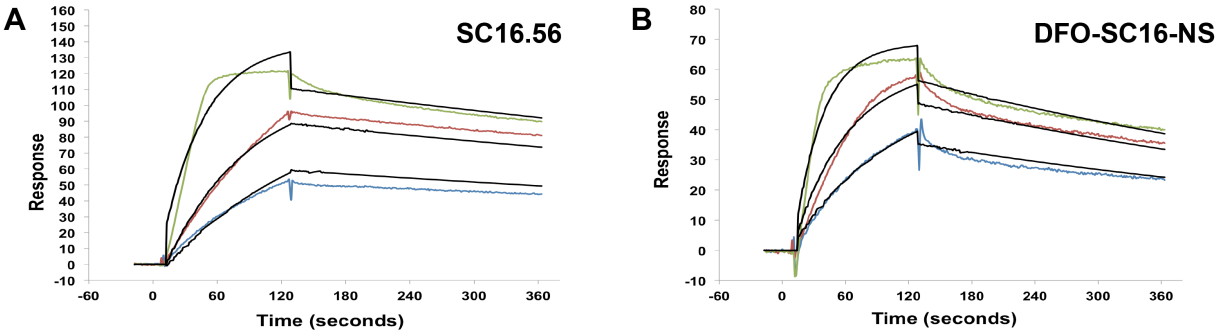

C

Construct	Loading	k_{on} (1/Ms)	k_{off} (1/Ms)	Rmax (RU)	Rmax/Loading	K_D(M)
Rova	154	5.0×10^{5}	7.8×10^{-4}	120	0.78	1.6×10^{-9}
Rova-NS	88	7.1×10^{5}	1.6×10^{-3}	60	0.68	2.3×10^{-9}

Figure S3a: Surface Plasmon Resonance DLL3 binding curves for (A) Un-modified SC16 versus (B) Non-site-selectively modified SC16 (DFO-SC16-NS); and (C) Kinetic constants for both the constructs.

Fig. S3b

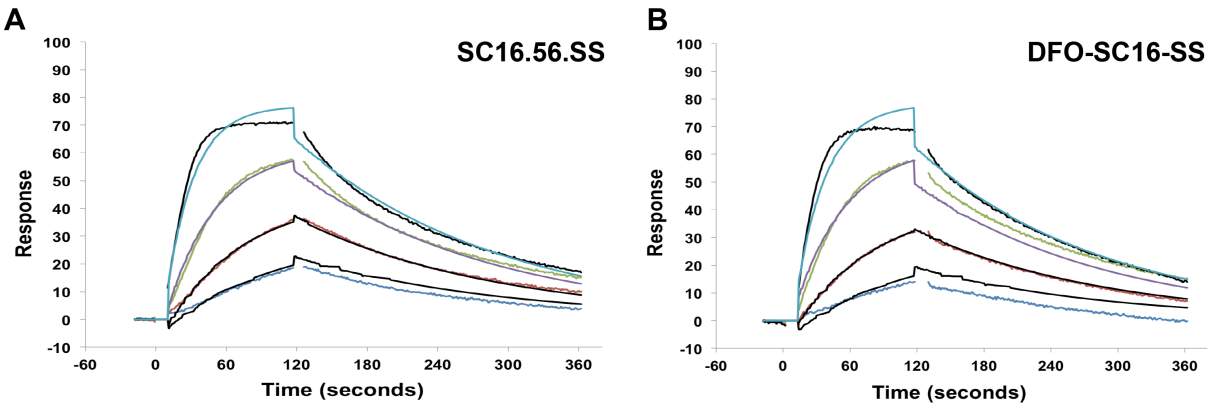

C

Construct	Loading	k_{on} (1/Ms)	k_{off} (1/Ms)	Rmax (RU)	Rmax/Loading	K_D(M)
Rova	126	1.5×10^{6}	5.9×10^{-3}	77	0.61	4.0×10^{-9}
Rova-SS	135	1.3×10^{6}	5.8×10^{-3}	76	0.56	4.7×10^{-9}

Figure S3b: Surface Plasmon Resonance DLL3 binding curves for (A) Un-modified SC16 versus (B) Site-selectively modified SC16 (DFO-SC16-SS); and (C) Kinetic constants for both the constructs.

Fig. S4

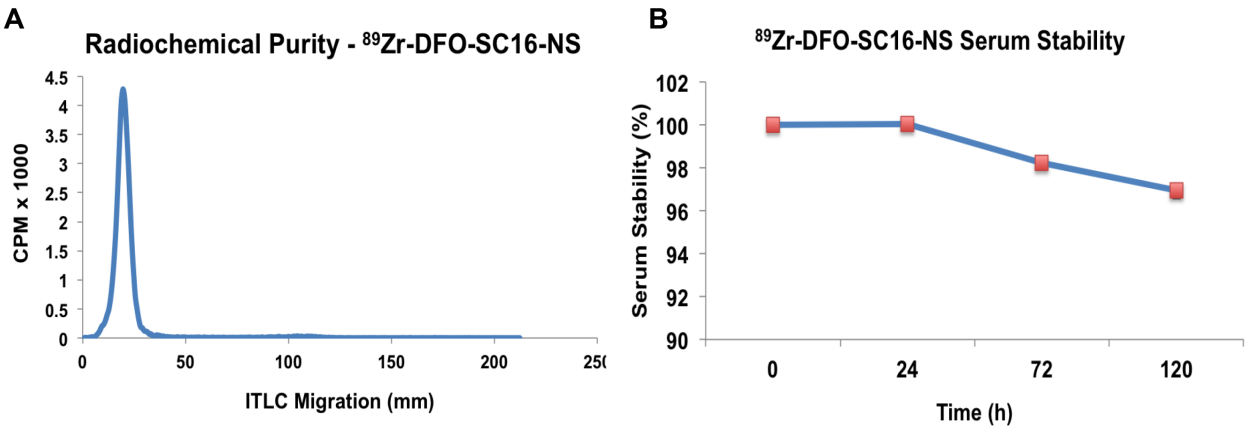

Figure S4. Physical characterization of the non-site-selectively modified SC16-based radioimmunoconjugate (^{89}Zr-DFO-SC16-NS). (A) The radiochemical purity of the size-exclusion purified ^{89}Zr-DFO-SC16-NS was tested via radio-TLC. The ratio of radioactivity at the baseline (~50 mm) versus the eluent front (~200 mm) indicates the purity of the preparation. **(B)** The purified ^{89}Zr-DFO-SC16-NS was evaluated for biochemical decomposition and demetallation of ^{89}Zr by incubating ~ 100 µCi of the radioimmunoconjugate in human AB type serum at 37 °C and shaking at 450 rpm. Radio-TLC experiments performed with the incubated radioimmunoconjugate demonstrated that ^{89}Zr-DFO-SC16-NS was > 95 % stable over a period of 5 days.

Fig. S5

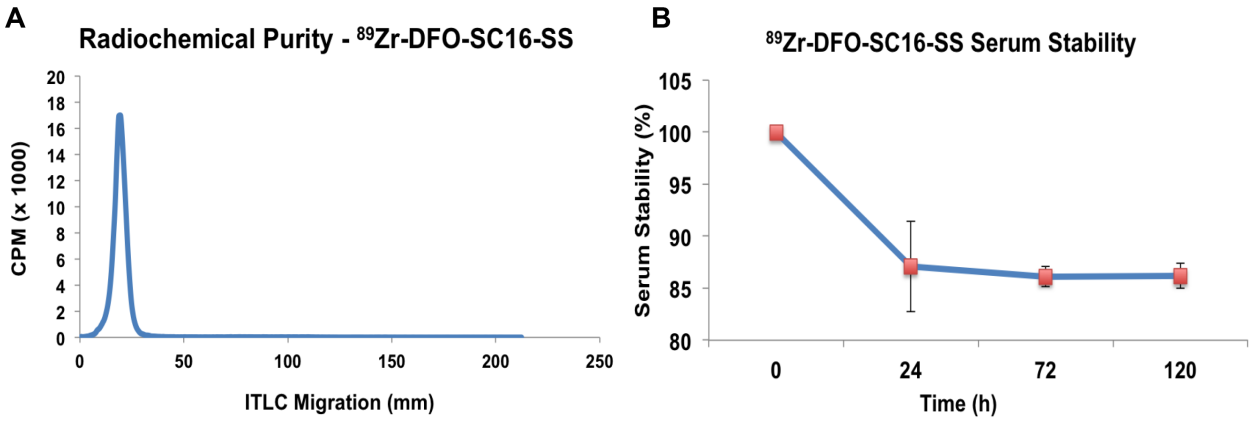

Figure S5. Physical characterization of the site-selectively modified SC16-based radioimmunoconjugate (^{89}Zr-DFO-SC16-SS). (A) The radiochemical purity of the size-exclusion purified ^{89}Zr-DFO-SC16-SS was tested via radio-TLC. The ratio of radioactivity at the baseline (~50 mm) versus the eluent front (~200 mm) indicates the purity of the preparation. **(B)** The purified ^{89}Zr-DFO-SC16-SS was evaluated for biochemical decomposition and demetallation of ^{89}Zr by incubating ~ 100 µCi of the radioimmunoconjugate in human AB type serum at 37 °C and shaking at 450 rpm. Radio-TLC experiments performed with the incubated radioimmunoconjugate demonstrated that ^{89}Zr-DFO-SC16-SS was > 85 % stable over a period of 5 days.

Fig. S6

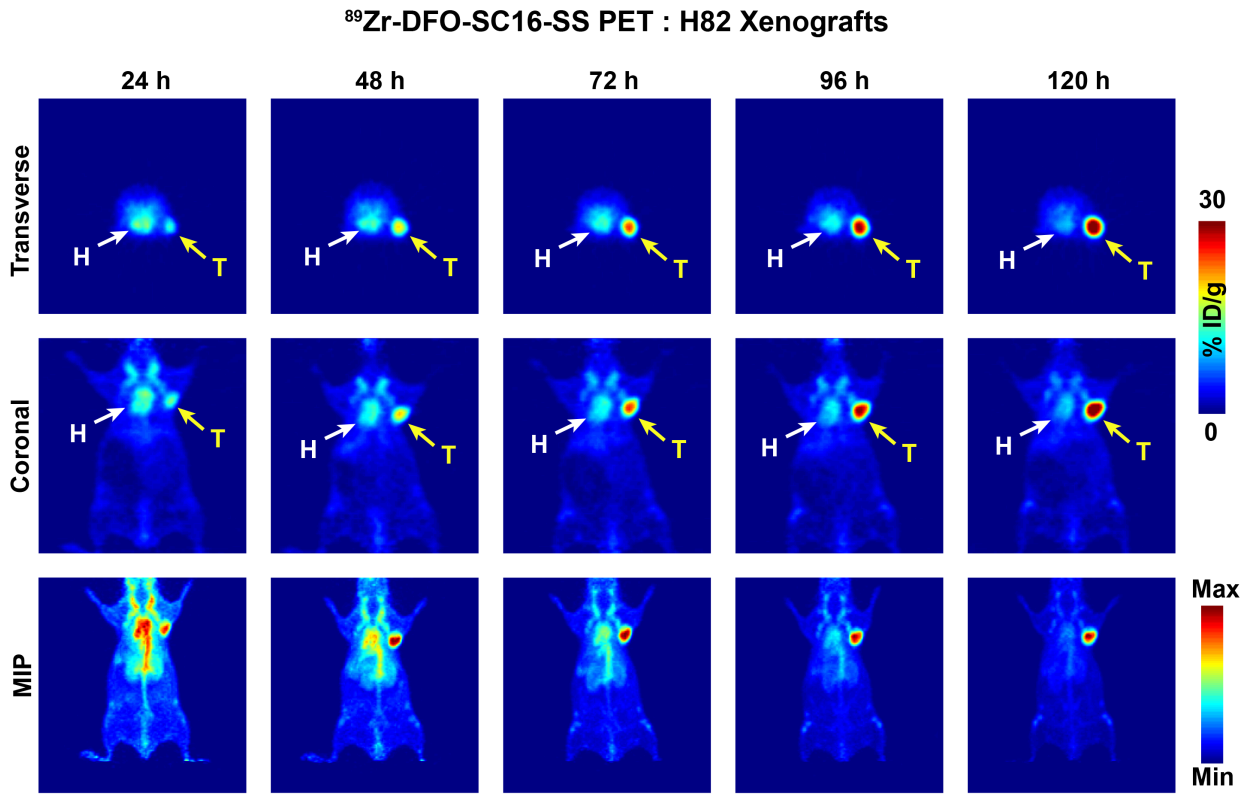

Figure S6. PET Imaging of subcutaneously xenografted H82 tumors with ^{89}Zr-DFO-SC16-SS. PET images of ^{89}Zr-DFO-SC16-SS (9.25 – 11.1 MBq; 250 – 300 µCi, 31-38 µg in chelex-treated PBS) in an athymic nude mouse bearing subcutaneous H82 tumors xenografted on the right shoulder. PET imaging was performed at 24 h intervals up to 120 h post-injection of ^{89}Zr-DFO-SC16-SS. The lowermost panel represents maximum intensity projection (MIP) images for all corresponding time points of evaluation. A gradual accretion of the radioactivity in the tumor (T) was visualized with the progression of time from 24 h up to 120 h after the injection of the radiotracer. A concomitant decrease in the radioactivity was observed in the systemic circulation (H).

Table S1. *Ex vivo* biodistribution data for ^{89}Zr-DFO-SC16-SS versus time in mice bearing subcutaneous H82 xenografts (n = 4 for each time point). Mice were administered ^{89}Zr-DFO-SC16-SS [0.74-0.925 MBq, (20-25 μCi), 2.5-3 μg in 200 μL chelex-treated PBS] via lateral tail vein injection (t = 0). For the 72 h time point, an additional cohort of animals were given ^{89}Zr-DFO-SC16-SS with dramatically lowered specific activity (LSA), achieved by the co-injection of the standard dose of the ^{89}Zr-labeled construct mixed with a 100-fold excess of cold, unlabeled SC16.56.SS antibody.

	24 h	48 h	72 h	72h Block	96 h	120 h
Blood	11.70 ± 1.82	8.34 ± 1.22	9.04 ± 2.91	11.49 ± 1.67	8.24 ± 0.48	8.57 ± 2.06
Heart	3.32 ± 0.47	3.02 ± 0.89	2.66 ± 0.75	3.51 ± 0.41	2.42 ± 0.03	2.53 ± 0.56
Lungs	5.99 ± 0.95	3.11 ± 0.82	5.25 ± 2.28	4.92 ± 0.59	3.20 ± 0.25	3.33 ± 0.66
Liver	2.35 ± 0.42	3.22 ± 0.96	2.92 ± 1.07	3.56 ± 0.85	2.76 ± 0.53	2.64 ± 0.51
Spleen	2.18 ± 0.40	1.84 ± 0.21	1.89 ± 0.87	2.28 ± 0.38	2.01 ± 0.63	1.97 ± 0.71
Stomach	0.67 ± 0.17	1.04 ± 0.29	0.46 ± 0.09	0.88 ± 0.20	0.64 ± 0.09	0.69 ± 0.22
L. Intestine	0.55 ± 0.07	0.55 ± 0.20	0.39 ± 0.07	0.47 ± 0.14	0.36 ± 0.06	0.38 ± 0.05
S. Intestine	0.88 ± 0.12	0.82 ± 0.16	0.69 ± 0.18	0.72 ± 0.04	0.69 ± 0.05	0.72 ± 0.13
Kidneys	5.32 ± 0.38	4.91 ± 0.66	5.68 ± 1.07	7.46 ± 0.21	5.42 ± 0.65	6.24 ± 1.08
Muscle	0.85 ± 0.09	0.79 ± 0.14	0.79 ± 0.24	0.90 ± 0.12	0.68 ± 0.05	0.57 ± 0.13
Bone	1.98 ± 0.24	2.43 ± 0.72	2.44 ± 0.12	2.64 ± 0.37	2.90 ± 0.77	3.87 ± 0.54
Tail	1.65 ± 0.30	1.67 ± 0.33	1.30 ± 0.39	1.76 ± 0.22	1.62 ± 0.17	1.36 ± 0.22
Skin	2.62 ± 0.57	4.18 ± 1.40	3.21 ± 1.31	4.35 ± 1.68	4.37 ± 0.66	2.71 ± 0.25
Tumor	10.06 ± 3.48	12.13 ± 2.19	18.83 ± 4.42	7.15 ± 0.47	14.34 ± 2.76	27.31 ± 6.03

Fig. S7

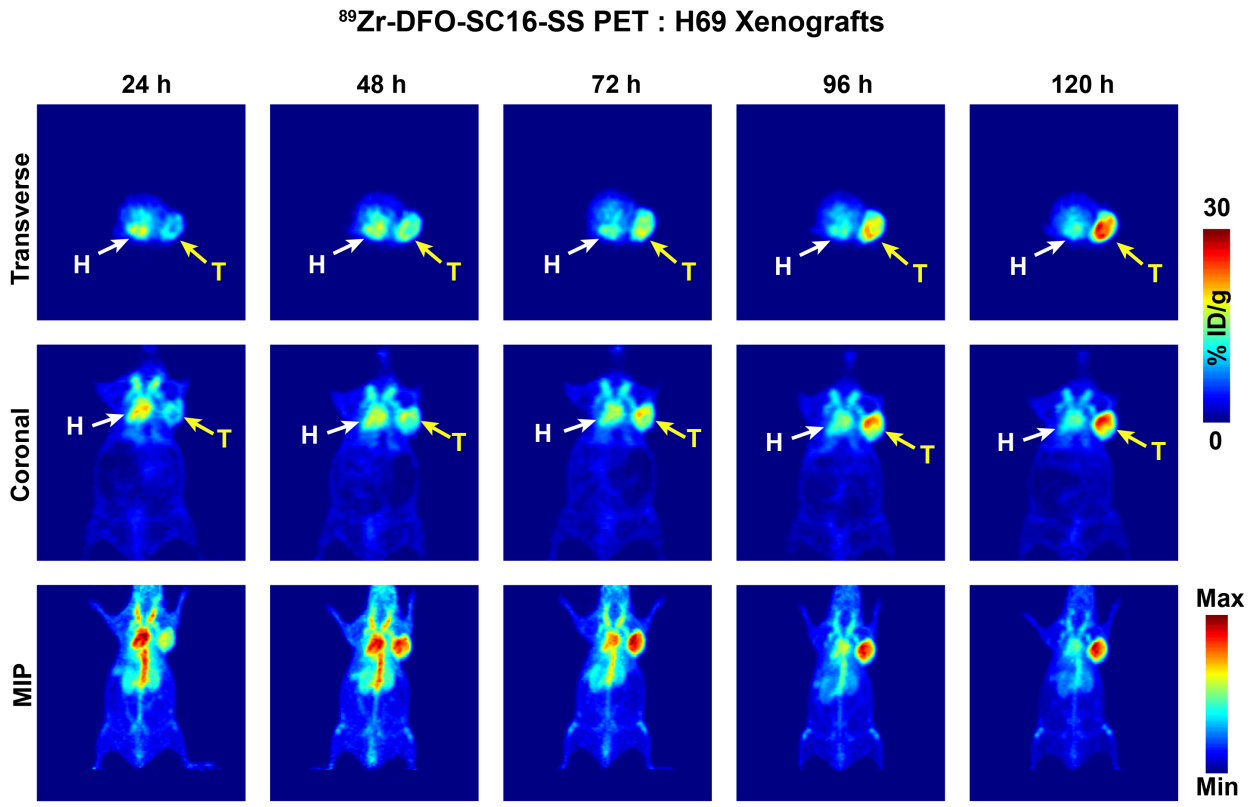

Figure S7. PET Imaging of subcutaneously xenografted H69 tumors with ^{89}Zr-DFO-SC16-SS. PET images of ^{89}Zr-DFO-SC16-SS (9.25 – 11.1 MBq; 250 – 300 µCi, 31-38 µg in chelex-treated PBS) in an athymic nude mouse bearing subcutaneous H69 tumors xenografted on the right shoulder. PET imaging was performed at 24 h intervals up to 120 h post-injection of ^{89}Zr-DFO-SC16-SS. The lowermost panel represents maximum intensity projection (MIP) images for all corresponding time points of evaluation. A gradual accretion of the radioactivity in the tumor (T) was visualized with the progression of time from 24 h up to 120 h after the injection of the radiotracer. A concomitant decrease in the radioactivity was observed in the systemic circulation (H).

Table S2. *Ex vivo* biodistribution data for ^{89}Zr-DFO-SC16-SS versus time in mice bearing subcutaneous H69 xenografts (n = 4 for each time point). Mice were administered ^{89}Zr-DFO-SC16-SS [0.74-0.925 MBq, (20-25 μCi), 2.5-3 μg in 200 μL chelex-treated PBS] via lateral tail vein injection (t = 0). For the 72 h time point, an additional cohort of animals were given ^{89}Zr-DFO-SC16-SS with dramatically lowered specific activity (LSA), achieved by the co-injection of the standard dose of the ^{89}Zr-labeled construct mixed with a 100-fold excess of cold, unlabeled SC16.56.SS antibody.

	24 h	**48 h**	**72 h**	**72h Block**	**96 h**	**120 h**
Blood	14.79 ± 2.14	11.52 ± 1.18	10.77 ± 1.10	15.02 ± 3.29	9.71 ± 1.30	7.28 ± 2.84
Heart	4.42 ± 1.39	3.78 ± 0.56	3.39 ± 0.31	4.75 ± 0.55	3.19 ± 0.47	2.22 ± 0.42
Lungs	6.46 ± 0.82	5.85 ± 1.65	4.77 ± 1.68	5.89 ± 0.72	3.71 ± 0.72	2.68 ± 1.30
Liver	3.10 ± 0.65	2.55 ± 0.42	2.33 ± 0.09	3.61 ± 1.33	3.23 ± 0.76	3.54 ± 1.07
Spleen	2.98 ± 0.59	3.23 ± 0.44	2.78 ± 0.47	4.01 ± 1.08	3.51 ± 0.52	3.09 ± 0.88
Stomach	0.89 ± 0.27	0.75 ± 0.19	0.83 ± 0.17	0.88 ± 0.25	0.62 ± 0.08	0.82 ± 0.21
L. Intestine	0.46 ± 0.09	0.43 ± 0.05	0.38 ± 0.07	0.41 ± 0.08	0.38 ± 0.04	0.41 ± 0.11
S. Intestine	0.97 ± 0.12	0.95 ± 0.19	0.86 ± 0.09	0.96 ± 0.26	0.90 ± 0.15	0.88 ± 0.15
Kidneys	7.87 ± 0.93	7.02 ± 0.70	7.06 ± 0.96	9.36 ± 1.49	7.59 ± 1.68	6.25 ± 1.17
Muscle	1.03 ± 0.19	0.85 ± 0.07	0.93 ± 0.20	1.12 ± 0.30	0.76 ± 0.10	0.70 ± 0.30
Bone	2.66 ± 0.46	3.15 ± 0.62	3.43 ± 0.59	3.39 ± 0.57	4.29 ± 1.24	4.31 ± 2.13
Tail	2.39 ± 0.64	1.77 ± 0.14	1.65 ± 0.35	2.11 ± 0.49	1.73 ± 0.17	1.54 ± 0.26
Skin	4.74 ± 0.93	4.65 ± 0.77	3.92 ± 0.38	6.29 ± 1.53	4.77 ± 1.22	4.23 ± 1.08
Tumor	7.96 ± 1.47	11.80 ± 2.63	13.91 ± 1.35	5.53 ± 1.51	13.19 ± 0.30	16.17 ± 5.84

Figure S8

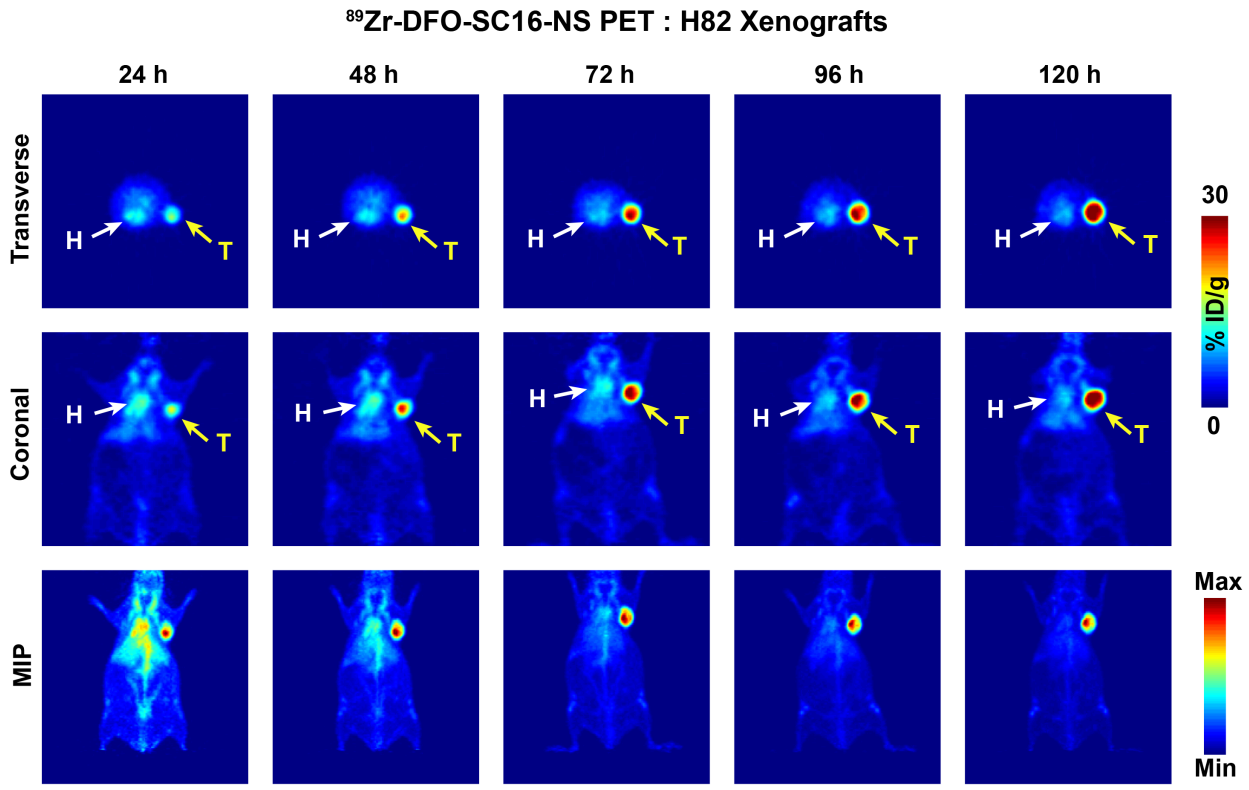

Figure S8. PET Imaging of subcutaneously xenografted H82 tumors with ^{89}Zr-DFO-SC16-NS. PET images of ^{89}Zr-DFO-SC16-NS (9.25 – 11.1 MBq; 250 – 300 µCi, 31-38 µg in chelex-treated PBS) in an athymic nude mouse bearing subcutaneous H82 tumors xenografted on the right shoulder. PET imaging was performed at 24 h intervals up to 120 h post-injection of ^{89}Zr-DFO-SC16-NS. The lowermost panel represents maximum intensity projection (MIP) images for all corresponding time points of evaluation. A gradual accretion of the radioactivity in the tumor (T) was visualized with the progression of time from 24 h up to 120 h after the injection of the radiotracer. A concomitant decrease in the radioactivity was observed in the systemic circulation (H).

Table S3. *Ex vivo* biodistribution data for ^{89}Zr-DFO-SC16-NS versus time in mice bearing subcutaneous H82 xenografts (n = 4 for each time point). Mice were administered ^{89}Zr-DFO-SC16-NS [0.81 MBq- 1.11 MBq; (22-30 μCi), 2.75- 3.75 μg in 200 μL chelex-treated PBS] via lateral tail vein injection (t = 0). For the 72 h time point, an additional cohort of animals were given ^{89}Zr-DFO-SC16-NS with dramatically lowered specific activity (LSA), achieved by the co-injection of the standard dose of the ^{89}Zr-labeled construct mixed with a 100-fold excess of cold, unlabeled SC16.56 antibody.

	24 h	48 h	72 h	72h Block	96 h	120 h
Blood	13.81 ± 1.09	9.45 ± 1.58	7.68 ± 0.46	10.86 ± 1.92	8.74 ± 1.42	6.92 ± 0.76
Heart	3.84 ± 0.44	2.90 ± 0.58	2.70 ± 0.55	3.25 ± 0.42	2.93 + 0.42	2.10 ± 0.40
Lungs	4.69 ± 0.42	3.36 ± 1.41	2.59 ± 0.34	4.31 ± 1.58	3.18 ± 0.64	2.84 ± 0.63
Liver	4.07 ± 0.25	4.12 ± 0.67	3.99 ± 0.83	3.37 ± 0.69	4.23 ± 1.16	4.03 ± 1.20
Spleen	3.86 ± 0.60	3.27 ± 0.32	3.58 ± 0.77	3.72 ± 0.69	4.07 ± 0.72	3.01 ± 0.21
Stomach	0.75 ± 0.21	0.78 ± 0.22	0.75 ± 0.17	0.95 ± 0.09	1.24 ± 0.74	0.59 ± 0.21
L. Intestine	0.59 ± 0.10	0.79 ± 0.22	0.55 + 0.10	0.66 ± 0.36	0.50 ± 0.03	0.44 ± 0.13
S. Intestine	0.98 ± 0.18	0.86 ± 0.13	0.80 ± 0.20	1.00 ± 0.18	1.03 ± 0.29	0.58 + 0.08
Kidneys	4.33 ± 0.37	3.82 ± 0.40	3.43 ± 0.37	4.09 ± 0.52	3.84 + 0.32	3.50 ± 0.50
Muscle	0.84 ± 0.04	0.88 ± 0.12	0.75 ± 0.05	0.94 ± 0.08	0.79 ± 0.17	0.56 ± 0.03
Bone	2.44 ± 0.48	5.33 ± 0.79	5.80 ± 1.03	3.64 ± 0.45	6.04 ± 1.84	3.67 + 1.98
Tail	3.39 ± 0.43	2.12 ± 0.19	2.02 ± 0.21	2.40 ± 1.20	1.99 ± 0.18	1.78 = 0.54
Skin	4.12 ± 0.78	3.48 ± 0.42	3.17 ± 0.65	3.34 ± 0.39	3.32 ± 0.74	3.00 = 0.17
Tumor	7.87 ± 1.23	13.16 ± 2.97	13.38 + 3.06	5.71 ± 0.80	14.07 ± 2.15	19.48 = 4.77

Fig. S9

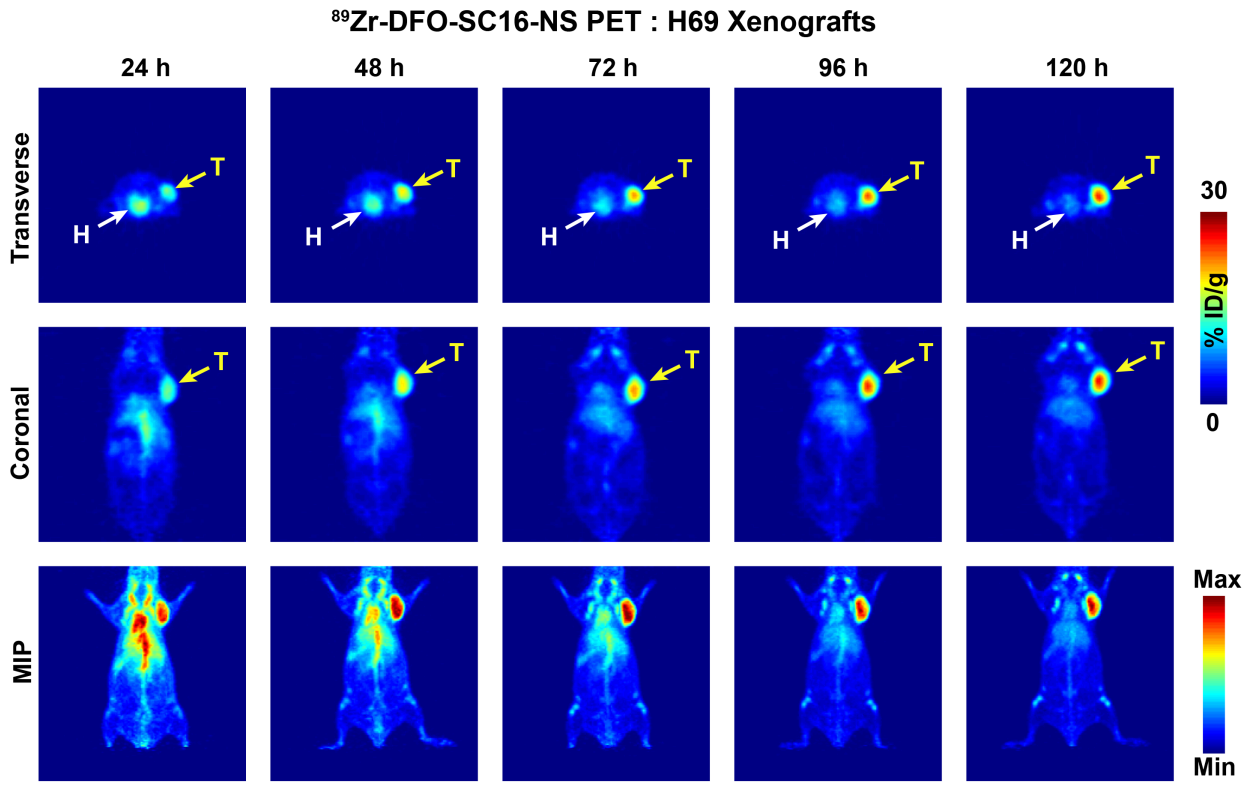

Figure S9. PET Imaging of subcutaneously xenografted H69 tumors with ^{89}Zr-DFO-SC16-NS. PET images of ^{89}Zr-DFO-SC16-NS (9.25 – 11.1 MBq; 250 – 300 µCi, 31-38 µg in chelex-treated PBS) in an athymic nude mouse bearing subcutaneous H69 tumors xenografted on the right shoulder. PET imaging was performed at 24 h intervals up to 120 h post-injection of ^{89}Zr-DFO-SC16-NS. The lowermost panel represents maximum intensity projection (MIP) images for all corresponding time points of evaluation. A gradual accretion of the radioactivity in the tumor (T) was visualized with the progression of time from 24 h up to 120 h after the injection of the radiotracer. A concomitant decrease in the radioactivity was observed in the systemic circulation (H).

Table S4. *Ex vivo* biodistribution data for ^{89}Zr-DFO-SC16-NS versus time in mice bearing subcutaneous H69 xenografts (n = 4 for each time point). Mice were administered ^{89}Zr-DFO-SC16-NS [0.81 MBq- 1.11 MBq; (22-30 μCi), 2.75- 3.75 μg in 200 μL chelex-treated PBS] via lateral tail vein injection (t = 0). For the 72 h time point, an additional cohort of animals were given ^{89}Zr-DFO-SC16-NS with dramatically lowered specific activity (LSA), achieved by the co-injection of the standard dose of the ^{89}Zr-labeled construct mixed with a 100-fold excess of cold, unlabeled SC16.56 antibody.

	24 h	48 h	72 h	72h Block	96 h	120 h
Blood	12.61 ± 2.17	12.36 ± 2.47	10.88 ± 1.48	11.90 ± 1.18	9.22 ± 0.87	7.23 ± 0.28
Heart	3.93 = 1.06	3.75 ± 0.85	3.76 ± 0.44	4.06 ± 0.62	2.75 ± 0.60	2.58 + 0.08
Lungs	4.69 + 0.99	6.10 ± 1.85	5.40 ± 1.32	5.40 ± 0.96	3.99 ± 0.99	2.61 ± 0.71
Liver	6.67 ± 0.84	5.29 ± 0.69	4.75 ± 0.49	4.80 ± 0.54	5.33 ± 1.94	3.67 ± 0.26
Spleen	3.88 ± 0.54	4.29 ± 2.39	6.12 ± 1.01	5.43 ± 0.94	4.93 ± 0.60	3.64 ± 0.41
Stomach	1.73 ± 0.47	1.04 ± 0.15	0.86 ± 0.30	0.48 + 0.13	0.77 ± 0.05	0.49 ± 0.10
L. Intestine	1.10 ± 0.42	1.06 ± 0.36	0.57 ± 0.06	0.71 ± 0.14	0.55 ± 0.05	0.46 ± 0.10
S. Intestine	1.76 ± 0.23	1.05 ± 0.10	0.75 ± 0.11	0.69 + 0.09	0.94 ± 0.08	0.77 ± 0.11
Kidneys	4.32 ± 0.67	4.48 ± 0.37	4.41 ± 0.32	4.65 ± 0.39	3.89 ± 0.35	3.45 ± 0.24
Muscle	1.22 ± 0.19	1.10 ± 0.08	0.99 ± 0.14	0.93 ± 0.05	0.82 ± 0.09	0.71 ± 0.04
Bone	4.33 ± 0.12	5.11 ± 1.41	8.99 ± 1.76	4.98 ± 0.97	6.20 + 1.23	7.79 ± 3.53
Tail	2.51 ± 0.11	2.09 ± 0.12	2.03 ± 0.08	2.39 ± 0.36	2.25 ± 0.17	2.22 ± 0.36
Skin	7.57 ± 1.09	5.58 ± 0.71	4.09 ± 0.58	4.10 ± 0.38	4.27 = 0.77	4.17 ± 0.30
Tumor	10.07 ± 2.52	11.96 ± 2.65	13.04 ± 4.42	5.26 ± 0.57	16.34 = 2.14	13.30 ± 3.17

Fig. S10

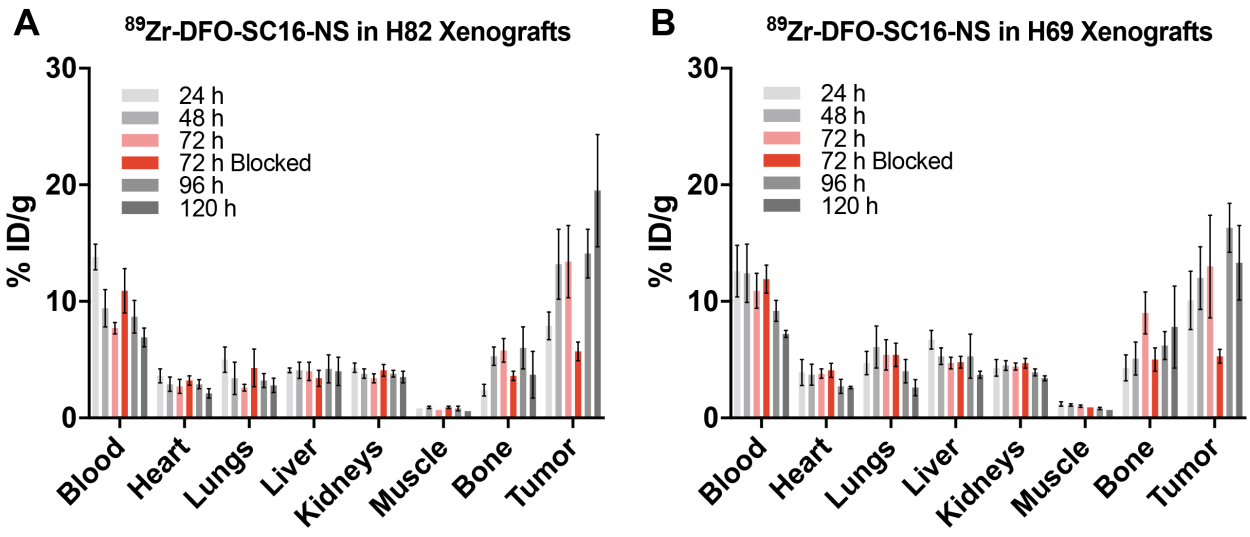

Figure S10. Biodistribution of non-site-selectively labeled ^{89}Zr-SC16-DFO-NS in subcutaneous xenograft models of SCLC. Biodistribution of ^{89}Zr-DFO-SC16-NS after lateral tail vein injection [0.81 MBq- 1.11 MBq; (22-30 μCi), 2.75- 3.75 μg in 200 μL chelex-treated PBS] in **(A)** H82 xenograft bearing mice; and **(B)** H69 xenograft bearing mice. The tumoral uptake of ^{89}Zr-DFO-SC16-NS could be blocked at 72 h by the co-injection of a 100-fold excess of the unlabeled SC16 antibody. Concordant with the level of DLL3 expression and consistent with the observations for the site-selectively labeled SC16-radioimmunoconjugate, a higher uptake of the radioimmunoconjugate was found in H82 tumors.

Table S5. A comparison of the tumor-to-background uptake activity concentration ratios of ^{89}Zr-DFO-SC16-SS vs. ^{89}Zr-DFO-SC16-NS in tissues of H82 xenografts.

	^{89}Zr-DFO-SC16-SS	**^{89}Zr-DFO-SC16-NS**
Tumor/Blood	3.2 ± 1.0	2.8 ± 0.8
Tumor/Heart	10.8 ± 3.4	9.3 ± 2.9
Tumor/Lung	8.2 ± 2.4	6.9 ± 2.3
Tumor/Liver	10.4 ± 3.0	4.8 ± 1.9
Tumor/Spleen	13.8 ± 5.8	6.5 ± 1.6
Tumor/Stomach	39.7 ± 15.5	32.8 ± 14.3
Tumor/Large Intestine	72.6 ± 19.1	44.0 ± 16.8
Tumor/Small Intestine	37.9 ± 10.9	33.4 ± 9.4
Tumor/Kidneys	4.4 ± 1.2	5.6 ± 1.6
Tumor/Muscle	47.5 ± 15.0	35.0 ± 8.8
Tumor/Bone	7.1 ± 1.8	5.3 ± 3.1
Tumor/Skin	10.1 ± 2.4	6.5 ± 1.6

Fig. S11

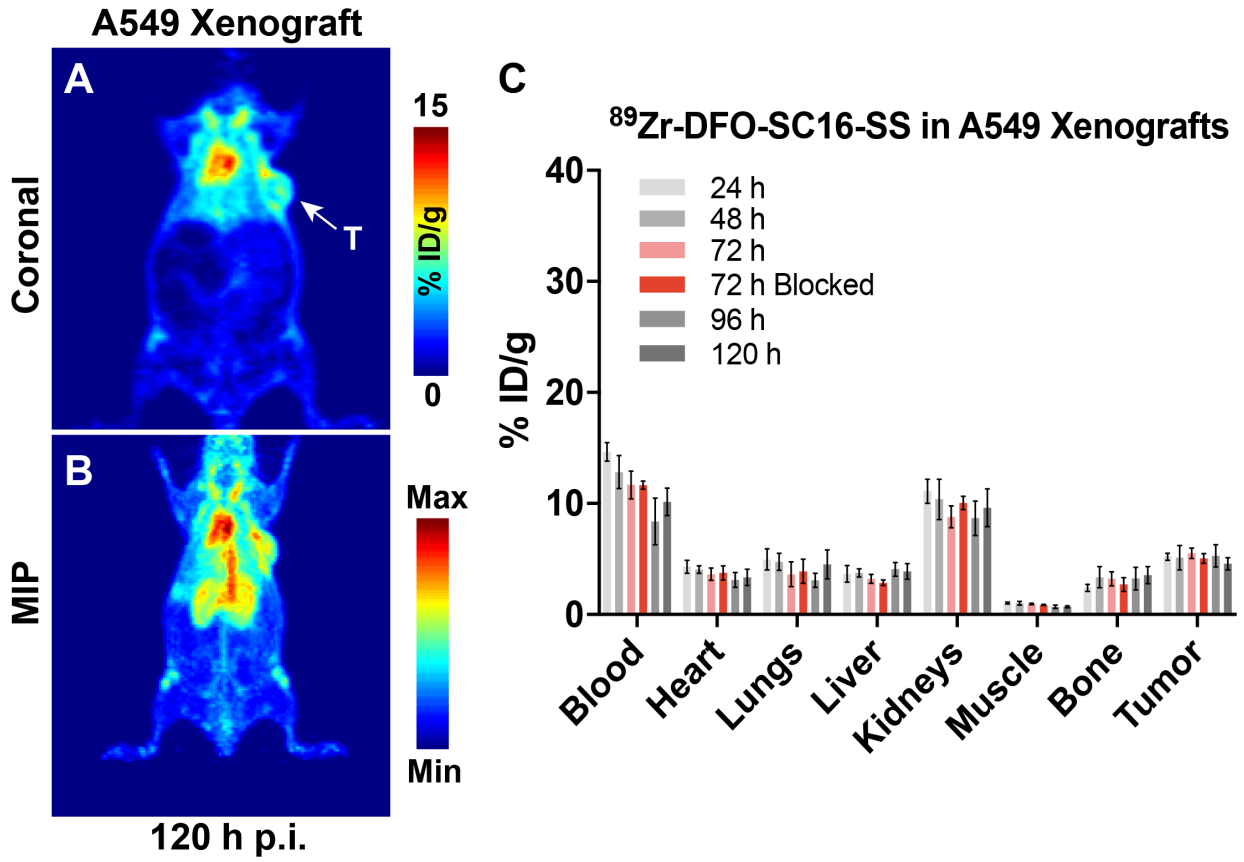

Figure S11. PET imaging and biodistribution of ^{89}Zr-DFO-SC16-SS in A549 xenograft bearing mice. PET images **(A)** Coronal slice and **(B)** Maximum Intensity Projection (MIP) of ^{89}Zr-DFO-SC16-SS in an athymic nude mouse xenografted with DLL3-negative A549 tumors on the right shoulder. Biodistribution studies **(C)** in mice (n=4 animals per time point) bearing subcutaneously xenografted A549 tumors revealed minimal uptake upto ~ 5 % ID/g, that could be attributed to enhanced permeability and retention in the leaky vasculature of the tumors.

Table S6: *Ex vivo* biodistribution data for ^{89}Zr-DFO-SC16-SS versus time in mice bearing subcutaneous DLL3-negative A549 xenografts (n = 4 for each time point). Mice were administered ^{89}Zr-DFO-SC16-SS [0.74-0.925 MBq, (20-25 μCi), 2.5-3 μg in 200 μL chelex-treated PBS] via lateral tail vein injection (t = 0). For the 72 h time point, an additional cohort of animals were given ^{89}Zr-DFO-SC16-SS with dramatically lowered specific activity (LSA), achieved by the co-injection of the standard dose of the ^{89}Zr-labeled construct mixed with a 100-fold excess of cold, unlabeled SC16 antibody. However, the blocking did not impact the non-specific uptake observed in the tumors at all the time points investigated.

	24 h	48 h	72 h	72h Block	96 h	120 h
Blood	14.65 ± 0.83	12.83 ± 1.48	11.68 ± 1.25	11.65 ± 0.37	8.36 ± 2.10	10.15 ± 1.23
Heart	4.30 ± 0.57	4.04 ± 0.33	3.63 ± 0.55	3.74 ± 0.63	3.07 ± 0.67	3.35 ± 0.74
Lungs	4.96 ± 0.96	4.74 ± 0.76	3.63 ± 1.12	3.89 ± 1.08	3.05 ± 0.62	4.52 ± 1.31
Liver	3.66 ± 0.74	3.75 ± 0.36	3.22 ± 0.39	2.86 ± 0.25	4.04 ± 0.62	3.89 ± 0.70
Spleen	3.70 ± 0.39	4.09 ± 0.55	3.33 ± 0.70	2.03 ± 1.08	3.10 ± 0.47	3.69 ± 0.13
Stomach	0.64 ± 0.09	0.88 ± 0.32	0.62 ± 0.23	0.90 ± 0.99	0.39 ± 0.15	0.52 ± 0.15
L. Intestine	0.57 ± 0.05	0.50 ± 0.09	0.37 ± 0.04	0.40 ± 0.15	0.34 ± 0.08	0.34 ± 0.03
S. Intestine	0.89 ± 0.13	0.99 ± 0.13	0.64 ± 0.10	0.65 ± 0.06	0.66 ± 0.22	0.67 ± 0.16
Kidneys	11.11 ± 1.08	10.37 ± 1.82	8.79 ± 0.98	10.06 ± 0.60	8.64 ± 1.55	9.62 ± 1.71
Muscle	1.02 ± 0.08	1.02 ± 0.17	0.95 ± 0.06	0.86 ± 0.04	0.65 ± 0.15	0.70 ± 0.09
Bone	2.41 ± 0.32	3.36 ± 0.96	3.21 ± 0.64	2.70 ± 0.62	3.20 ± 1.01	3.54 ± 0.76
Tail	1.98 ± 0.09	2.12 ± 0.30	1.63 ± 0.21	1.42 ± 0.20	1.28 ± 0.20	1.48 ± 0.18
Skin	6.13 ± 0.64	6.01 ± 0.42	4.17 ± 1.02	7.35 ± 2.11	3.50 ± 0.33	3.89 ± 0.34
Tumor	5.20 ± 0.32	5.11 ± 1.09	5.52 ± 0.46	5.06 ± 0.43	5.25 ± 1.00	4.57 ± 0.55

Fig. S12

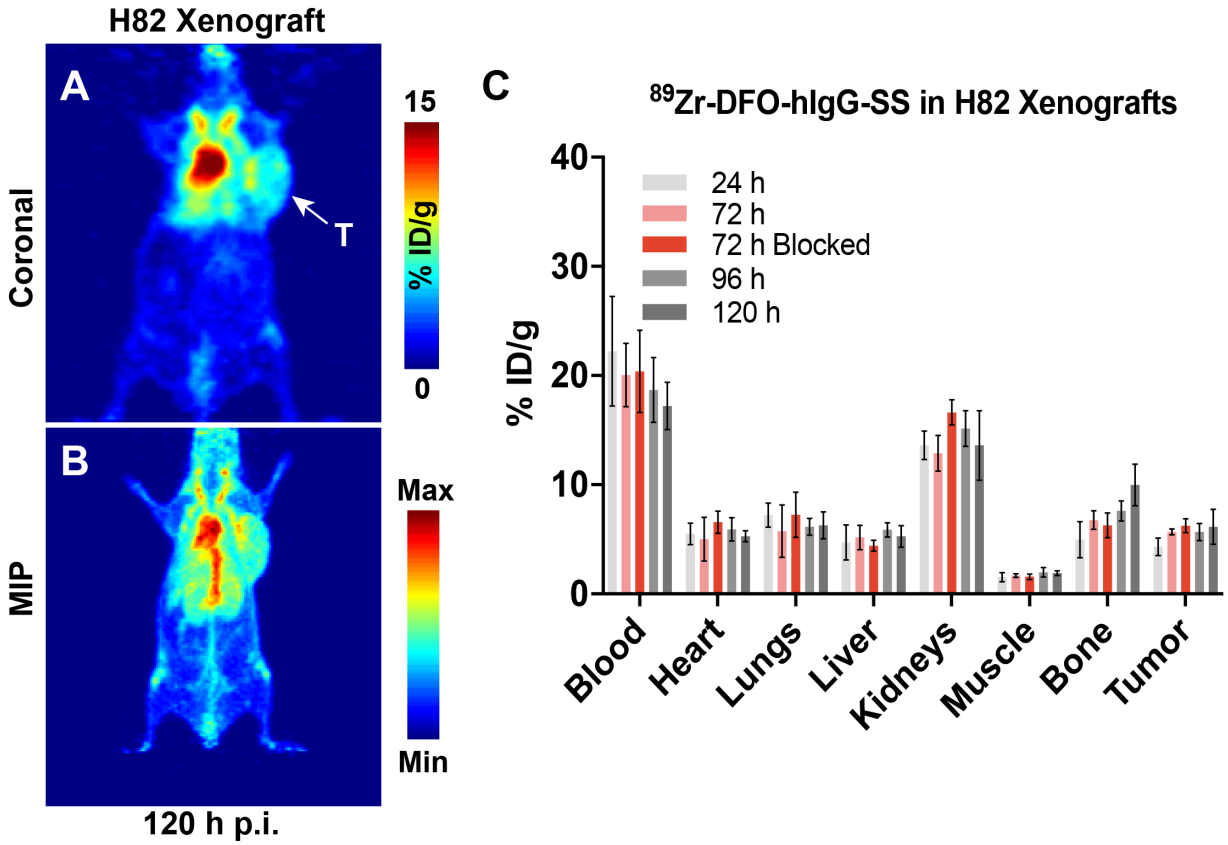

Figure S12. PET imaging and biodistribution of an isotype-matched non-specific ^{89}Zr-DFO-hIgG-SS radioimmunoconjugate in H82 xenograft bearing mice. PET images **(A)** Coronal slice and **(B)** Maximum Intensity Projection (MIP) of ^{89}Zr-DFO-hIgG-SS in an athymic nude mouse xenografted with DLL3-positive H82 tumors on the right shoulder. Biodistribution studies **(C)** in mice (n=4 animals per time point) bearing subcutaneously xenografted H82 tumors revealed a non-specific uptake upto ~ 6 % ID/g, that could be attributed to enhanced permeability and retention in the leaky vasculature of the tumors.

Table S7: *Ex vivo* biodistribution data for ^{89}Zr-DFO-hIgG-SS versus time in mice bearing subcutaneous DLL3-positive H82 xenografts (n = 4 for each time point). Mice were administered ^{89}Zr-DFO-hIgG-SS [0.77-1.14 MBq, (21-31 μCi), 2.6-3.2 μg in 200 μL chelex-treated PBS] via lateral tail vein injection (t = 0). For the 72 h time point, an additional cohort of animals were given ^{89}Zr-DFO-hIgG-SS with dramatically lowered specific activity (LSA), achieved by the co-injection of the standard dose of the ^{89}Zr-labeled construct mixed with a 100-fold excess of cold, unlabeled isotype-matched antibody.

	24 h	72 h	72h Block	96 h	120 h
Blood	22.23 ± 5.03	20.05 ± 2.89	20.38 ± 3.77	18.67 ± 2.97	17.21 ± 2.16
Heart	5.50 ± 0.99	5.02 ± 1.99	6.57 ± 1.01	5.91 ± 1.07	5.29 ± 0.50
Lungs	7.10 ± 0.98	5.76 ± 2.40	7.25 ± 2.06	6.16 ± 0.77	6.28 ± 1.24
Liver	4.71 ± 1.60	5.17 ± 1.11	4.40 ± 0.50	5.88 ± 0.65	5.27 ± 0.99
Spleen	4.65 ± 1.21	4.23 ± 0.38	4.86 ± 1.23	4.45 ± 0.64	4.73 ± 0.69
Stomach	1.18 ± 0.57	0.99 ± 0.35	1.74 ± 0.50	2.02 ± 0.14	1.22 ± 0.32
L. Intestine	1.20 ± 0.97	0.44 ± 0.06	0.55 ± 0.13	0.74 ± 0.18	0.66 ± 0.03
S. Intestine	1.20 ± 0.23	1.20 ± 0.16	1.30 ± 0.14	1.48 ± 0.19	1.38 ± 0.30
Kidneys	13.60 ± 1.30	12.89 ± 1.63	16.63 ± 1.15	15.15 ± 1.62	13.60 ± 3.18
Muscle	1.54 ± 0.41	1.68 ± 0.16	1.57 ± 0.25	1.98 ± 0.43	1.90 ± 0.21
Bone	4.97 ± 1.64	6.76 ± 0.84	6.27 ± 1.13	7.61 ± 0.92	9.98 ± 1.90
Tail	2.13 ± 0.89	2.70 ± 0.45	2.30 ± 0.40	2.81 ± 0.34	2.86 ± 0.37
Skin	6.92 ± 2.23	5.46 ± 0.96	5.81 ± 1.32	6.70 ± 1.68	6.66 ± 1.04
Tumor	4.31 ± 0.81	5.67 ± 0.27	6.25 ± 0.63	5.67 ± 0.78	6.15 ± 1.59

Fig. S13

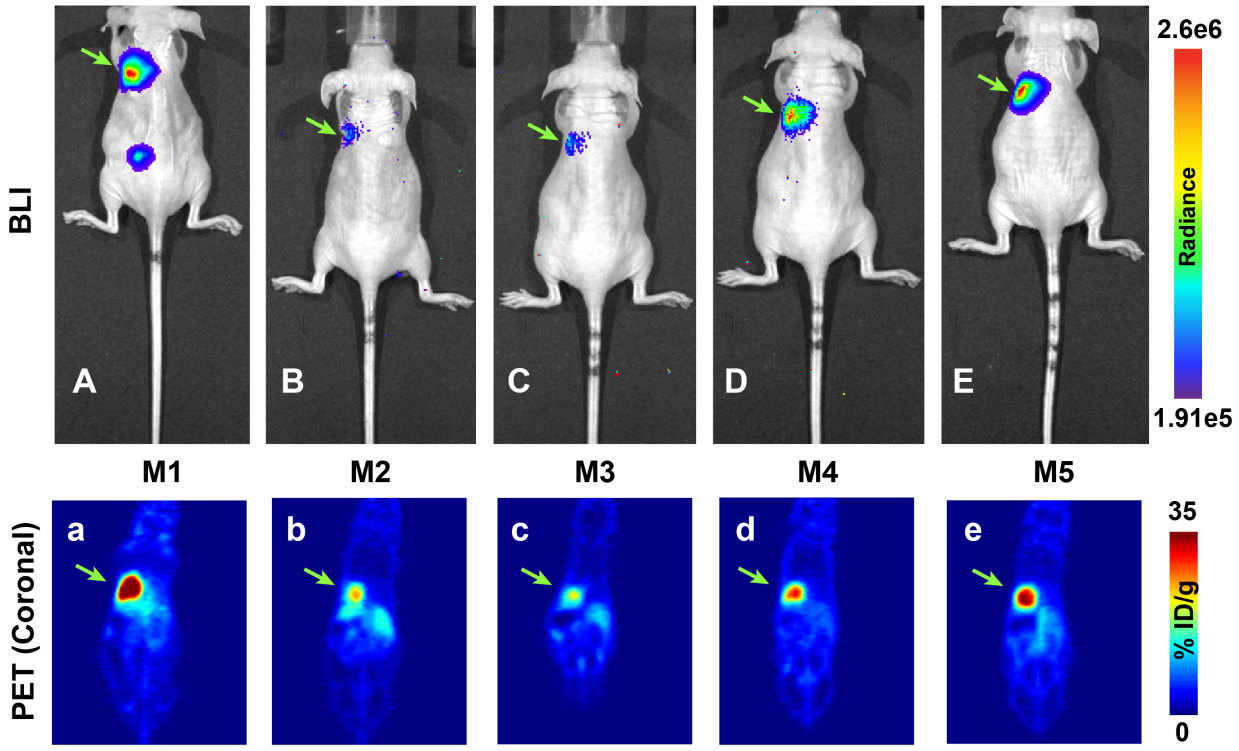

Figure S13. Bioluminescence and ^{89}Zr-DFO-SC16-SS PET imaging of mice bearing orthotopically xenografted luc-H82 tumors in the left lung. Mice were screened via bioluminescence imaging (BLI) prior to PET imaging with ^{89}Zr-DFO-SC16-SS to identify those that had tumors and to non-invasively assess the tumor burden in these animals based on the radiance arising from the luc-H82 tumor cells. **(A-E)** The upper panel shows 5 mice imaged via bioluminescence. The lower panel **(a-e)** shows PET images obtained at 120 h after the injection of ^{89}Zr-DFO-SC16-SS (9.25 – 11.1 MBq; 250 – 300 µCi, 31-38 µg in chelex-treated PBS) via the lateral tail vein of corresponding mice shown in the upper panel. The intenstity of the PET signal (in the lower panel) bears a strong concordance with the bioluminescence signal (in the upper panel) indicating tumor burden (green arrows) in the left lungs of the orthotopic xenograft model. Radiance = photons/sec/cm^2/steridian.

Fig. S14

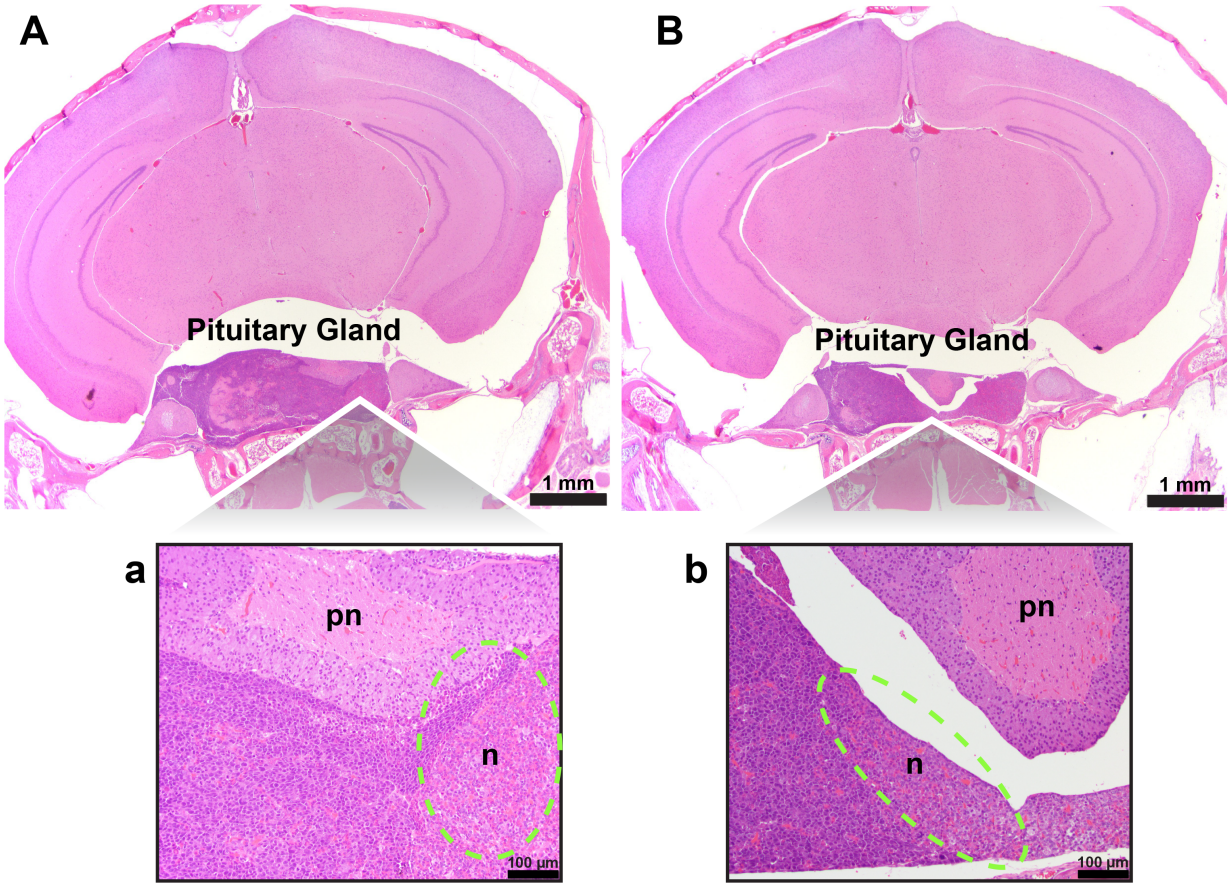

Figure S14. Histopathological analysis of a portion of the skull in mice from the metastatic cohort to examine the pituitary gland for infiltration by SCLC tumor cells. **(A-B)** H&E-stained sections of the decalcified skull from 2 representative mice from the metastatic experimental cohort showing the overall architecture of the hypophysis and the pituitary gland tissues; **(a-b)** A magnified view of pituitary gland showing neoplastic cells (n) (green dashed oval areas) effacing the pars distalis and unilaterally infiltrating portions of the pars intermedia, while leaving the pars nervosa (pn) unaffected.

Fig. S15

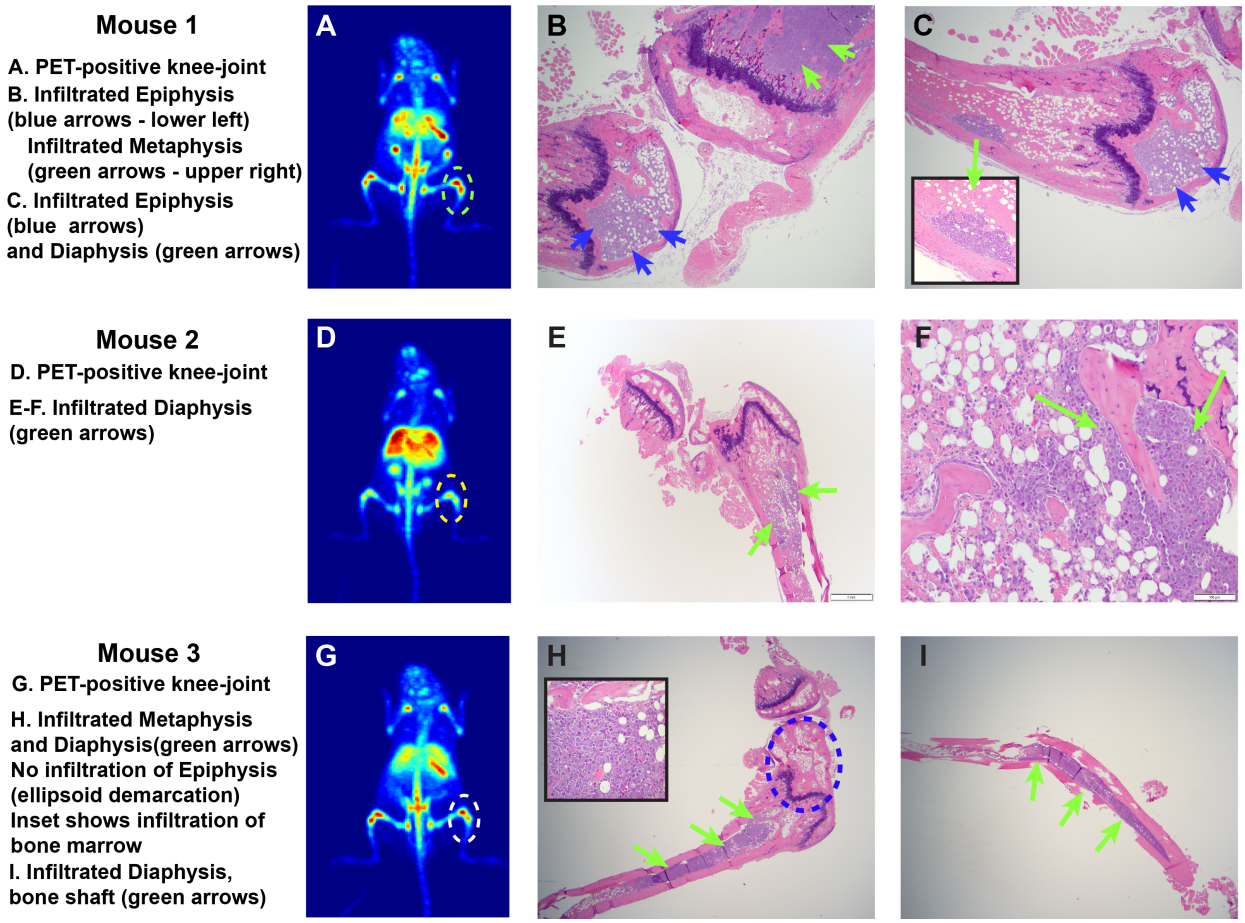

Figure S15. Cross examination of ^{89}Zr-DFO-SC16-SS PET and histopathology of the bones in mice to confirm metastatic spread of SCLC. Each mouse in this figure represents a case for the discord between PET imaging and histopathology from 3 separate categories of bone metastases documented in the distant organ metastatic model developed for SCLC. Mouse 1 showed – **(A)** a high-intensity PET signal from the region of the knee-joint; **(B)** a histopathologically positive epiphysis in one and metaphysis in the other bone meeting at the joint, but no presence of infiltrated cells within the joint region itself; **(C)** a PET-negative tibia shows the presence of infiltrated cells in the diaphysis – magnified view seen in the inset; Mouse 2 showed – **(D)** a relatively low-intensity PET signal from the region of the knee-joint; **(E-F)** a heavily infiltrated diaphysis (indicated by green arrows); No corresponding PET signal was observed to highlight the presence of the infiltrated cells in this region of the leg bones in this mouse; Mouse 3 showed – **(G)** a high-

intensity PET signal from the region of the knee-joint; **(H-I)** an absence of infiltrating cells in the joint region and the epiphysis (region demarcated by the blue ellipsoid) of the two bones at the joint. The metaphysis, diaphysis and the shaft bone of the tibia were found to be heavily infiltrated, however, no corresponding PET signal was observed to indicate the presence of metastases in these regions of the infiltrated bone tissue.

Fig. S16

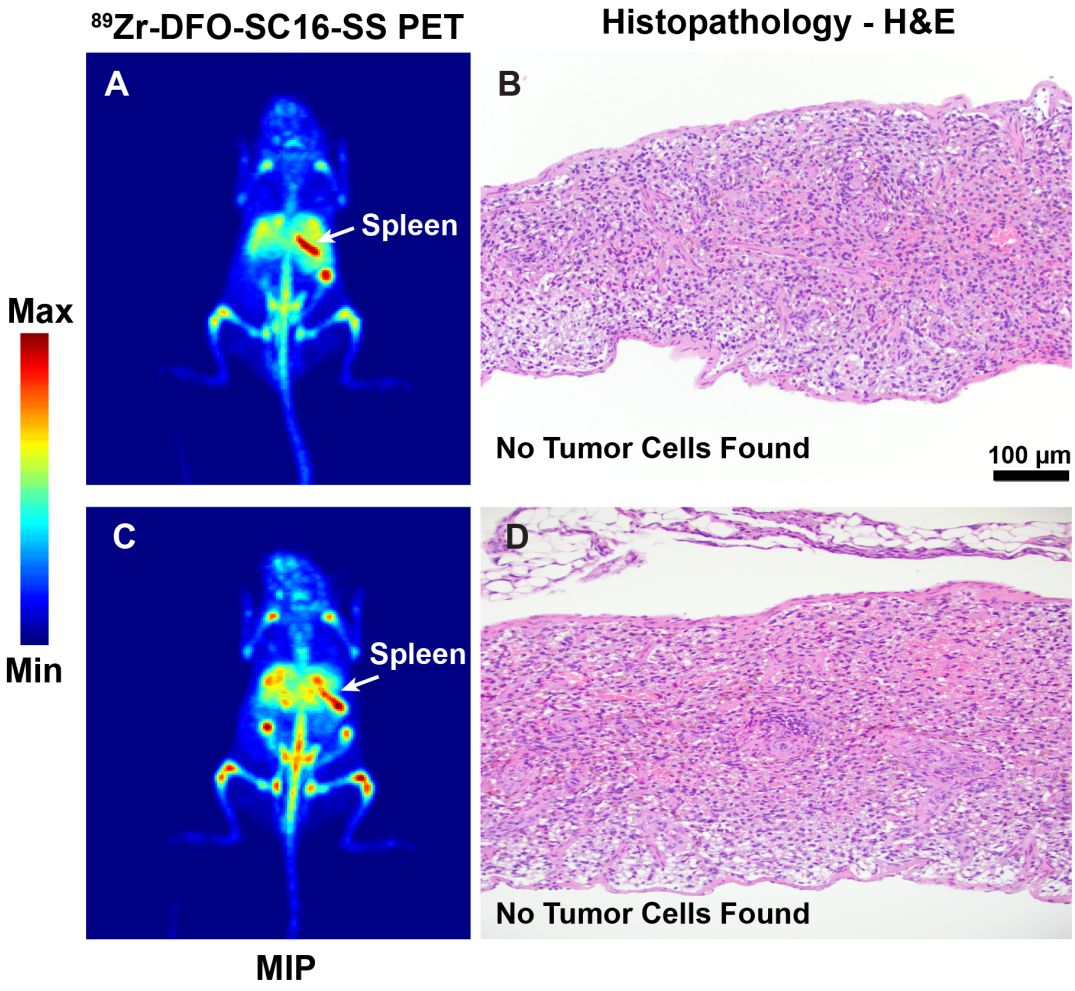

Figure S16. Histopathological examination of spleens that were positive on DLL3 PET in a metastatic model for SCLC. **(A)** Maximum Intenstity Projection (MIP) of a mouse from the metastatic model cohort showing low tumor burden in the liver but, high intensity PET signal arising from the spleen. **(B)** H&E-stained section of the PET-positive spleen shown in A. No metastatic SCLC cells were found in the spleen to yield such a high PET signal. **(C)** Maximum Intenstity Projection (MIP) of another mouse from the metastatic model cohort showing low tumor burden in the liver but, high intensity PET signal arising from the spleen. **(D)** H&E-stained section of the PET-positive spleen shown in C. No metastatic SCLC cells were found in the spleen to yield such a high PET signal. In the absence of any infiltrating cells and aggregation of the radioimmunoconjugate, the high spleen uptake may be caused by a mouse strain-specific biology.

Fig. S17

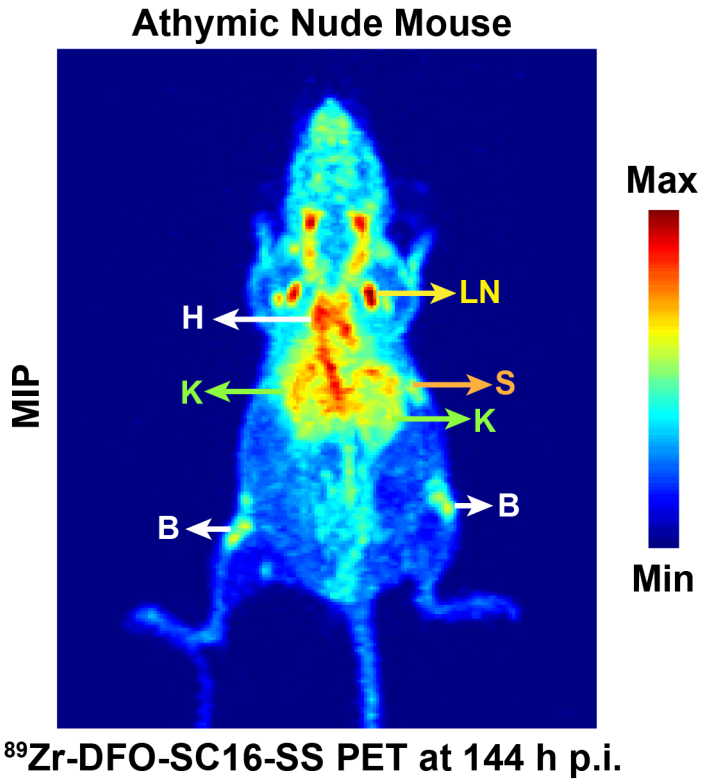

Figure S17. PET image of an athymic nude mouse injected with ^{89}Zr-DFO-SC16-SS from the same preparation batch as that injected in the cohort of 16 NSG mice used for the PET imaging of distant organ metastases of SCLC. PET image of a representative athymic nude mouse 144 h after the injection of ^{89}Zr-DFO-SC16-SS [7.4 MBq/200 µCi of in 200 µL chelex-treated PBS] via the lateral tail vein. 3 nude mice were injected with the same number of luc-H82 cells weeks prior to the use of the NSG strain of mice to develop a metastatic model for SCLC; however, these mice did not show presence of metastases via PET and BLI imaging. In the absence of an *in vivo* target sink, the ^{89}Zr-DFO-SC16-SS can be seen floating within circulation (H) even at 144 h after the injection of the radioimmunoconjugate. Non-specific uptake of radioactivity was observed in background tissues such as the kidneys (K), bone (B), lymph nodes (LN) and spleen (S).

Fig. S18

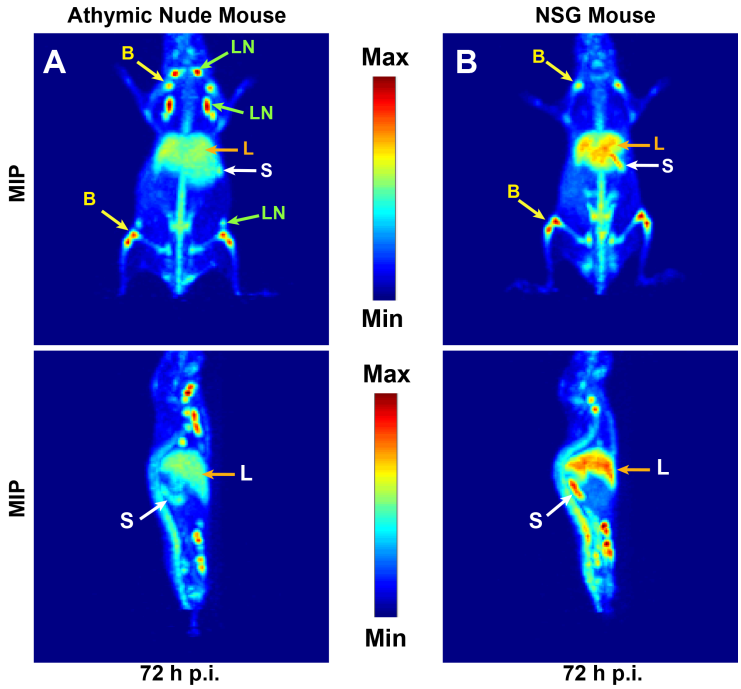

Figure S18. PET images showing the differential *in vivo* distribution patterns of the same preparation of ^{89}Zr-DFO-SC16-NS in two different mouse strains. (A) Maximum Intensity Projection (MIP) PET images (Upper panel – ventral view; Lower panel – sagittal view) of a non-tumor bearing athymic nude mouse at 72 h after the injection of ^{89}Zr-DFO-SC16-NS via the lateral tail vein. In the absence of an in vivo target sink, the radioimmunoconjugate was cleared predominantly via the hepatobiliary route through the liver (L). Some non-specific concentration of activity was seen in non-target organs such as the lymph nodes (LN), spleen (S) and bones (B); **(B)** Maximum Intensity Projection (MIP) PET images (Upper panel – ventral view; Lower panel – sagittal view) of a non-tumor bearing NSG (Nod Scid Gamma) mouse at 72 h after the injection of ^{89}Zr-DFO-SC16-NS via the lateral tail vein. In the absence of an in vivo target sink, the radioimmunoconjugate was cleared predominantly via the hepatobiliary route through the liver (L). Apparently higher non-specific concentration of activity was seen in non-target organs such as the spleen (S) and bones (B). No lymph node associated concentration of radioactivity was observed in this mouse strain.

Fig. S19

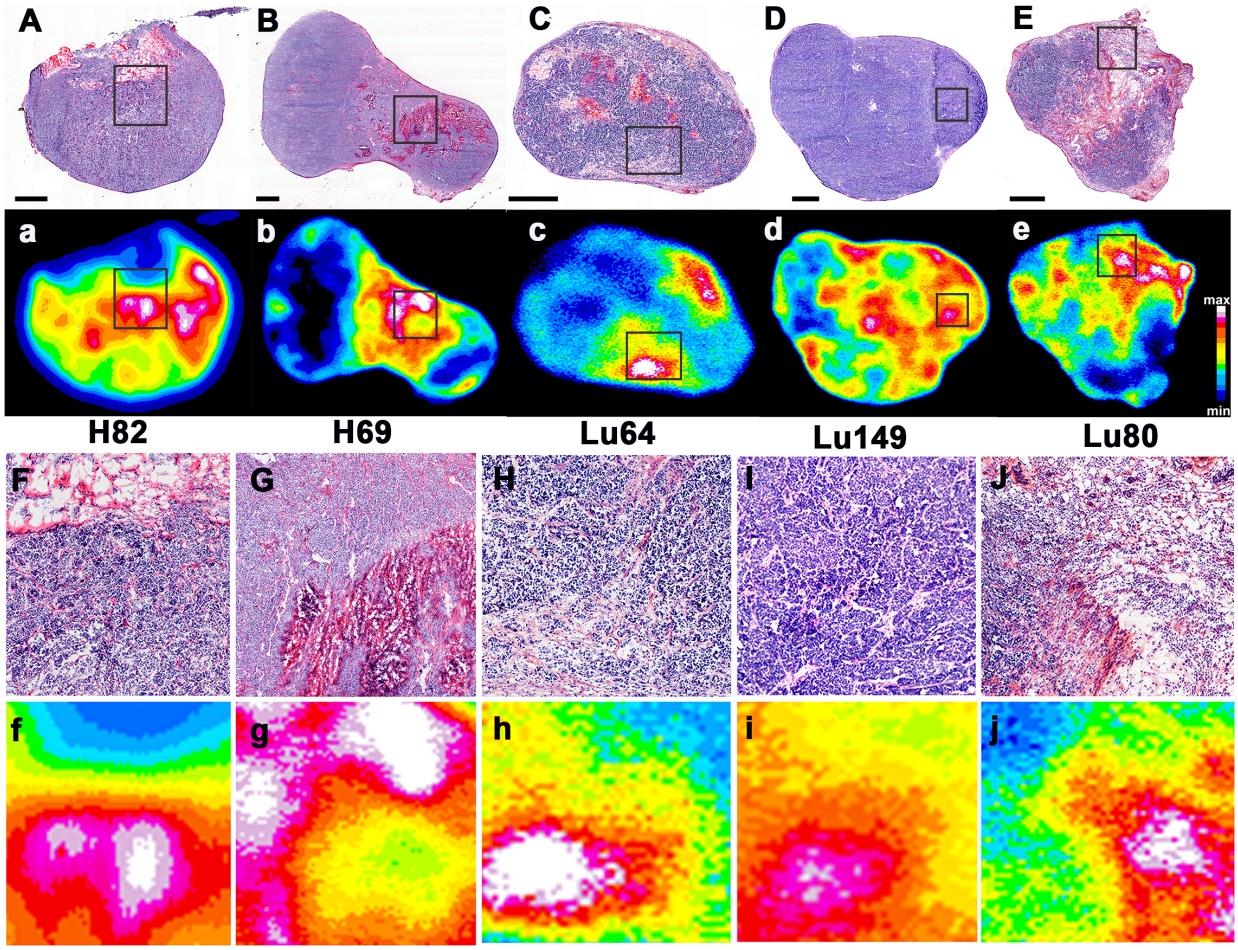

Figure S19. ***Ex vivo*** **analyses of subcutaneously xenografted SCLC tumors.** H&E-staining (A-E) and autoradiography (a-e) of sections from SCLC tumors - (A,a) H82; (B,b) H69; (C,c) Lu64; (D,d) Lu149; (E,e) Lu80; The autoradiography images show the distribution of ^{89}Zr-DFO-SC16-SS within a single tumor section 120 h after its *in vivo* administration via lateral tail vein injection in subcutaneously xenografted tumors. The data are normalized to the maximum intensity pixel within each section to show the relative spatial distribution, rather than absolute uptake; (F-J and f-j) Magnified views of the boxed regions of the tumor section shown in the upper two panels to visualize more detail. The intratumoral distribution of ^{89}Zr-DFO-SC16-SS showed some differences between the tumor models examined. In the cell line derived tumors (H82 and H69), there was a clear association of ^{89}Zr in viable tumor regions, with lesser uptake in regions with

extensive necrosis. However, heterogeneity within the viable regions was also observed, which likely results from a combination of variable vascular delivery and limited diffusion of the radioimmunoconjugate within the tumor. This distribution pattern was somewhat different in the Lu64 and Lu149 tumors, where an association with stroma-rich tumor regions suggests a distribution governed largely by vascular delivery. However, regions of viable tumor tissue showed a higher concentration of ^{89}Zr than neighboring necrotic regions, suggesting some specific retention of the antibody. The distribution in the Lu80 tumor appeared to be more closely related to tumor necrotic regions, suggesting that the ^{89}Zr-DFO-SC16-SS uptake in this model was dominated by passive diffusion and EPR effect with little specific binding seen in viable tumor regions (4).

REFERENCES:

1. Sharma SK, Sevak KK, Monette S, Carlin SD, Knight JC, Wuest FR, et al. Preclinical 89Zr Immuno-PET of High-Grade Serous Ovarian Cancer and Lymph Node Metastasis. J Nucl Med. 2016;57:771-6.
2. Reubi JC, Kvols LK, Waser B, Nagorney DM, Heitz PU, Charboneau JW, et al. Detection of somatostatin receptors in surgical and percutaneous needle biopsy samples of carcinoids and islet cell carcinomas. Cancer Res. 1990;50:5969-77.
3. Viola-Villegas NT, Sevak KK, Carlin SD, Doran MG, Evans HW, Bartlett DW, et al. Noninvasive Imaging of PSMA in prostate tumors with (89)Zr-Labeled huJ591 engineered antibody fragments: the faster alternatives. Mol Pharm. 2014;11:3965-73.
4. Heneweer C, Holland JP, Divilov V, Carlin S, Lewis JS. Magnitude of enhanced permeability and retention effect in tumors with different phenotypes: 89Zr-albumin as a model system. J Nucl Med. 2011;52:625-33.